New 3D velocity model (mTAB3D) for absolute hypocenter location in southern Iberia and the westernmost Mediterranean.

José Luis Sánchez-Roldán[1], José A. Álvarez-Gómez[1], José J. Martínez-Díaz[1,2], Paula Herrero-Barbero[3], Hector Perea[4], Juan V. Cantavella[5], and Lucía Lozano[5]

[1]Department of Geodynamics, Stratigraphy and Paleontology, Complutense University of Madrid, Madrid, Spain.

[2]Geosciences Institute (IGEO-CSIC), Madrid, Spain.

[3]Geosciences Barcelona (GEO3BCN-CSIC), Barcelona, Spain.

[4]Institut de Ciències del Mar - CSIC, Barcelona, Spain.

[5]Spanish Seismic Network, Instituto Geográfico Nacional (IGN), Madrid, Spain.

Corresponding author: José Luis Sánchez-Roldán (jl.sanchez.roldan@ucm.es)

Key Points:

- New 3D velocity model for southern Iberia and the westernmost Mediterranean.
- Relocation of hypocenters in the Trans-Alboran Shear Zone and seismotectonic analysis.
- Seismotectonic analysis of a continuous catalog in Eastern Betics Shear Zone, and the Al-Hoceima seismic sequence (2016).

Abstract

The Trans-Alboran Shear Zone is one of the most seismically active areas in the westernmost Mediterranean, where a wide variety of tectonic domains have developed within the context of oblique convergence between Eurasia and Africa plates. In this region, earthquakes occur close to seismogenic structures, some of them large enough to cause damaging events. In addition, the diversity of tectonic domains implies a lateral variation of seismic wave propagation, which could affect the hypocenter reliability if not addressed during the location procedure. In this work, we present mTAB3D, a new 3D P-wave velocity model that accounts for the lateral heterogeneity of our study area. To test this model, we used arrival times from the Spanish Seismic Network catalog and performed two non-linear absolute location inversions: the first comprises all the seismicity detected during 2018-2022 in the Eastern Betics Shear Zone; the second one consists of the earthquakes recorded during the Al-Hoceima seismic sequence (2016). We compare our results against hypocenters computed with a 1D velocity model of the region (mIGN1D) and observe that mTAB3D achieves better clustering near active structures and lower epicentral uncertainties. Moreover, hypocenters obtained with mTAB3D show notable reliability even in scenarios of a low azimuthal gap, such as the 2016 Al-Hoceima sequence. The new catalogs computed with our model help us to infer possible genetic relations between seismicity and source faults within our study area and can be used as an additional tool when looking into prior seismic sequences.

Plain Language Summary

The convergence between Africa and Eurasia plates developed the Trans-Alboran Shear Zone, where earthquakes are quite frequent. Here, seismicity is controlled by the main active structures,

and some of them can trigger large earthquakes (M≥6.0). The tectonic complexity of the study area implies that seismic waves after an earthquake do not propagate equally in every direction, which may produce mislocations when a laterally homogeneous model is used. Due to this, we have developed a new 3D velocity model (mTAB3D) that accounts for this heterogeneity. We tested mTAB3D by locating earthquakes from two catalogs from the Spanish Seismic Network that occurred in our study area and compared the results to those obtained using a 1D model. Broadly, our results show lower uncertainties and locations closer to the possible fault sources, even in scenarios of unfavorable distribution of seismic stations. We conclude that mTAB3D can be used to obtain reliable hypocenters for seismotectonic studies within the westernmost Mediterranean.

1 Introduction

The need for a more precise location of earthquakes within areas with clear evidence of recent active tectonics is critical, not only to improve tectonic interpretation but also for seismic hazard analysis. However, to achieve an accurate solution, we usually face some issues that could hamper our results: (1) the number and spatial distribution of seismic stations, (2) the number and uncertainty in the seismic wave phase arrivals, and (3) how suitable is the velocity model used in the hypocenter inversion (Husen & Hardebeck, 2010). Altogether, assessing the hypocentral absolute location of earthquakes with the lowest possible uncertainty is the primary goal of recent studies that review earthquake catalogs. Some works strive for better precision and accuracy by relocating the earthquakes using new techniques or improved velocity models (Diehl et al., 2021; Lomax & Savvaidis, 2022).

In the Iberian peninsula and its surroundings, the former task has been fulfilled in different regions by modeling the 3D variation of the seismic waves in the subsurface at multiple scales from local (Theunissen et al., 2018; Sánchez-Roldán et al., 2021) to regional (Moudnib et al., 2015; Lozano et al., 2020), or even greater scale (Arroucau et al., 2021). These models have allowed us to estimate the influence of lateral velocity variations over the earthquake location within the region of interest. Furthermore, this procedure is essential in studies that seek to associate earthquakes with specific tectonic sources.

The westernmost Mediterranean, and particularly the Alboran basin, is a tectonically complex region characterized by a shallow (<30 km), low-moderate seismicity (Stich et al., 2003). However, there is evidence in the historical and instrumental record of large earthquakes in this region along the Betic Cordillera, Alboran Sea, and Maghrebian margin: the 1518 Vera earthquake (EMS-98 VIII-IX), 1804 and 1910 Adra earthquakes (EMS-98 intensity VIII-IX), and the 1994 – 2004 Al-Hoceima earthquakes (Mw 5.9 and Mw 6.3 respectively) (Martínez-Solares & Mezcua, 2002; Biggs et al., 2006; Kariche et al., 2018). More recently, a Mw 6.4 struck the offshore area of Al-Hoceima on 2016/01/25 causing material damage and casualties (Buforn et al., 2017; Gràcia et al., 2019).

The shallow seismicity (depth < 50 km) is related to the deformation caused by the slow Africa-Eurasia NW-SE convergence (Serpelloni et al., 2007; De Mets et al., 2015), with a rate of ~4-6 mm/yr. The regional active tectonics is characterized by the transcurrent fault systems active since at least late Tortonian times (7-9 Ma) (Bourgois et al., 1992; Comas et al., 1992; Woodside and Maldonado, 1992). In this context, we observe the Trans Alboran shear zone (TASZ) (De Larouzière et al., 1988), and its northwards continuation onshore, the Eastern Betics

Shear Zone (EBSZ) (Bousquet, 1979; Silva et al., 1993). Both systems cut from SW to NE in the Alboran Basin and connect the Iberian and Maghrebian margins.

In this work, we present a new 3D velocity model that comprises the region bounded by the southern Iberian margin, the Alboran basin, and the North African margin. After that, we test the suitability of the model by relocating two earthquake datasets corresponding to two subregions within the TASZ and the EBSZ: the first includes the seismicity registered during 2018-2022 in the Eastern Betics, and the second the earthquakes detected during the Al-Hoceima 2016 seismic sequence. The reliability of the model and relocations are evaluated by comparing the parameters and uncertainties of the hypocenters to previous results computed with a 1D velocity model (Mezcua and Martínez-Solares, 1983). Finally, a seismotectonic analysis of each region is carried out based on the new hypocenters and how they may be related to nearby active faults that could act as sources.

2 Geodynamic and tectonic setting

The Gibraltar Arc and Betic-Rif cordillera are placed between the African and Eurasian plates in the westernmost Mediterranean (Fig. 1). A slow convergence at 4~6 mm/yr between these two plates is responsible for the complex tectonic features in this region (Seton et al., 2012; Vissers and Meijer, 2012).

The major geological features of the Alpine Betic-Rif orogenic system are:

- The Internal zones that belong to the Alboran Domain, which also can be subdivided into three equivalent tectonic complexes (from bottom to top on the Betics/Rif system): a) Nevado-Filabride only in the Betics and inferred to be the edge of the South Iberian paleomargin; b) the Alpujarride/Sebtide and c) the Malaguide/Ghomaride (Balanyá & García-Dueñas, 1987; Galindo-Zaldívar et al., 1989; Chalouan & Michard, 1990; Jabaloy et al., 1993; Bouyabaouene et al., 1995; Booth-Rea et al., 2015).
- The External zones composed of Mesozoic-Miocene sedimentary rocks deposited over the Maghrebian (Prerif, Mesorif, and Intrarif) and South Iberian (Subbetic, and Prebetic) margins, and the Flysch units over them (Crespo-Blanc & Frizon de Lamotte, 2006).
- Neogene basins with Miocene to Pliocene infill (e.g.: Guadalquivir, Granada, or Guadix-Baza among others) (Viseras et al., 2005), or Plio-Quaternary sediments like the Algero-Balearic and Alboran basins (Gómez de la Peña et al., 2021). The Alboran basin is traditionally subdivided into the West Alboran basin (WAB), South Alboran basin (SAB), and East Alboran basin (EAB), where the WAB reaches the maximum sedimentary thickness (~8 km) (Fernández-Ibáñez and Soto, 2017).

From the last ~35 Ma, slab subduction and western migration and the placement of the Alboran domain over the Maghrebian and Iberian paleomargins, are considered the main processes driving the tectonic evolution of the westernmost Mediterranean (Royden, 1993; Faccena et al., 2014). Although this is still a matter of debate, some geodynamic models involving mantle delamination (Calvert et al., 2000) with associated slab tearing (Booth-Rea et al., 2007; Mancilla et al., 2015a) are proposed in this context of slab roll-back extension (Lonergan & White, 1997; Faccena et al., 2004; Spakman & Wortel, 2004) and possible clockwise rotation in subduction orientation (Chertova et al., 2014; van Hinsbergen et al., 2014). An NNW-oriented extension develops sedimentary basins in the region from the late Serravallian

to the late Tortonian. Later, since the late Miocene, a process of tectonic inversion causes an NW-SE shortening, resulting in structures resembling "basin and range" morphology (Weijermars, 1987; Montenat & d'Estevou, 1999; Meijninger & Vissers, 2006; Herrero-Barbero et al., 2020), where the extensional basins have been deformed and cut off by the occurrence of the TASZ and the EBSZ (De Larouzière, 1988).

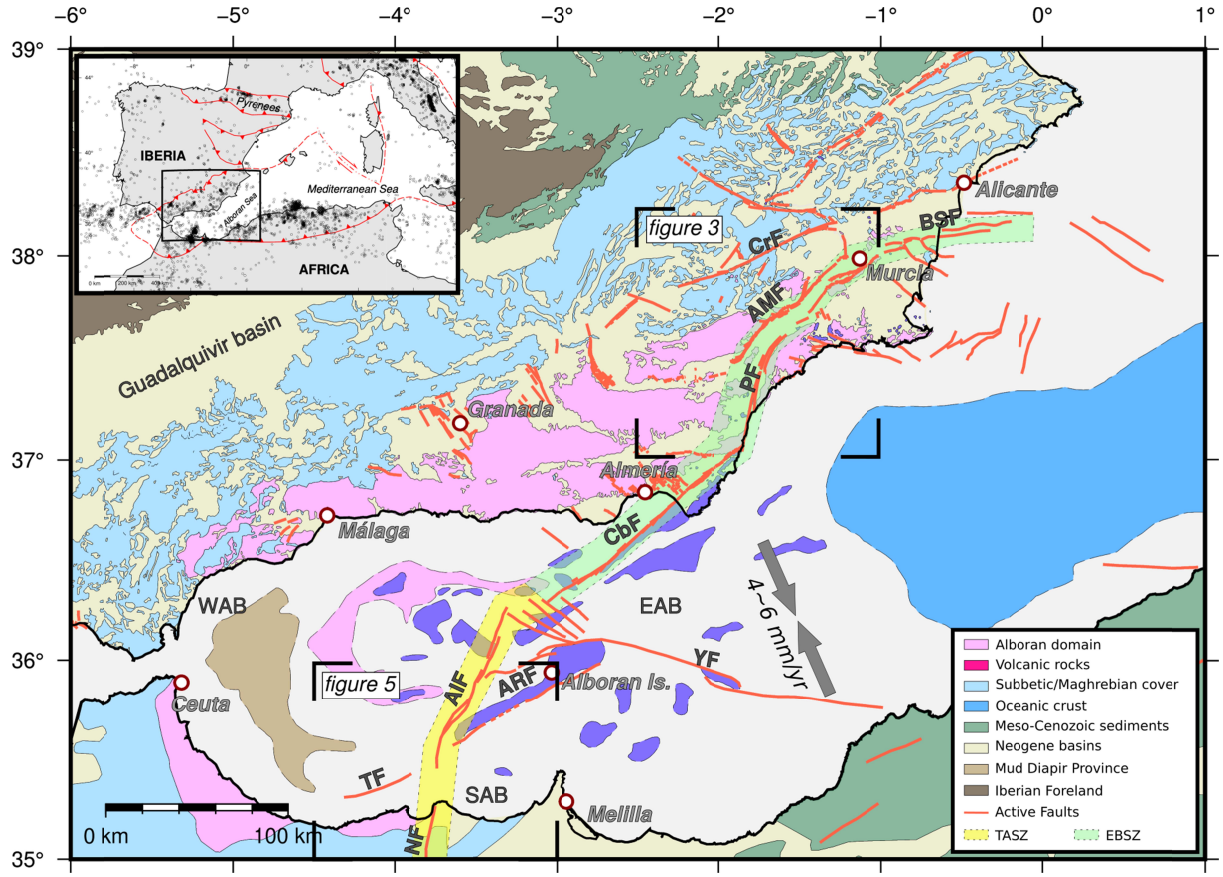

Figure 1

The TASZ and EBSZ comprise a system of strike-slip and reverse faults oriented from NNE-SSW to ENE-WSW, developed in that post-Miocene shortening stage and cut off from the Maghrebian to the South Iberian margins across the Alboran Basin, affecting both the basement and Neogene-Quaternary sediments of the area. According to GNSS data, the present-day transpressive tectonic regime is driven by a NNW-SSE shortening (Argus et al., 2011; Echeverria et al., 2013, Borque et al., 2019; Piña-Valdés et al., 2022), which is coherent with the kinematics on the major faults within the TASZ and EBSZ, as evidenced by field data, seismic profiles, or earthquake focal mechanisms (i.e., Stich et al., 2003, 2006; Giaconia et al., 2015; Martín et al., 2015; Moreno et al., 2016; Ferrater et al., 2017). Here, from south to north, the main crustal faults are: the Nekor fault (NF; Leblanc & Olivier, 1984), Trougout fault (TF; Lafosse et al., 2018), Al-Idrisi fault (AIF; Ammar et al., 2007), Alboran Ridge Front fault (ARF; Ballesteros et al., 2008), Yusuf fault (YF; Mauffret et al., 1987), Carboneras fault (CbF; Bousquet & Phillip, 1976), Palomares fault (PF; Völk, 1967), Alhama de Murcia fault (AMF; Montenat, 1973), Carrascoy fault (CF; Silva, 1993) and Bajo Segura fault (BSF; Montenat,

1977). Some of these faults, especially those across the Alboran basin, act as boundaries between different crustal domains (Gómez de la Peña et al., 2018) and constitute structured tectonic blocks with a diffuse and minor to moderate seismic activity (Rodríguez-Escudero et al., 2014; Grevemeyer et al., 2015). In this scenario, different studies have explored the possibility of large seismic ruptures propagating along various fault segments or even entire fault systems in the ESBZ (Gómez-Novell, et al., 2020; Herrero-Barbero, et al., 2021).

3 Materials and Methods

As previously stated, Alboran and south Iberia regions have a complex structure due to their complicated tectonic evolution. Thus, the suitability of the velocity model applied during the relocation is crucial for obtaining well-constrained hypocenter solutions (Husen and Hardebeck, 2010). Sometimes, relying on average seismic velocity models (1D models) could bias or offset the results. Because of that, some studies propose the use of 3D models that account for the lateral variation of velocity to tackle the mislocation of hypocenters caused by oversimplification of the crustal and mantle heterogeneities (Husen et al., 2003; Flanagan et al., 2007; Carannante et al., 2015; Matos et al., 2018; Theunissen et al., 2018; Lozano et al., 2020; Diehl et al., 2021).

3.1 mTABD3D: new regional 3D velocity model

In this paper, we present a 3D velocity model (hereafter mTAB3D) based on a compilation of geophysical and geological data of the study area (6ºW/1ºE/35ºN/39ºN) that accounts for the most relevant structures and their influence on the lateral variation of P-wave propagation, such as the two continental margins with different mountain ranges, or the most important sedimentary basins (Fig. 2).

During the modeling process, data related to the composition and structure at depth were used to model three regional surfaces:

- Topography/bathymetry: Taken from topography (Amante, C. & B.W. Eakins, 2009; NOAA National Geophysical Data Center, 2009) and bathymetry (GEBCO Compilation Group, 2022) data.
- Basement top: multichannel seismic reflection data (Rodríguez-Fernández et al., 2004; Medaouri et al., 2014; Haberland et al., 2017; Marín-Lechado et al., 2017; Martínez-García, et al., 2017; Gómez de la Peña et al., 2018; d'Acremont et al., 2020; Gómez de la Peña et al., 2021), and 2D gravity modeling profiles (Amores Lahidalga et al., 2002; García-Castellanos et al., 2002; Jiménez-Pintor et al., 2002; Sanz de Galdeano et al., 2007; Alfaro et al., 2008; Insua-Arévalo, 2008; Pedrera et al., 2020).
- Moho discontinuity: wide-angle seismic data (Booth-Rea et al., 2018; Gómez de la Peña et al., 2020), P-wave receiver function (Mancilla et al., 2015a; Mancilla & Díaz, 2015), deep seismic sounding (Díaz & Gallart, 2009), 2D gravity modeling profiles (Insua-Arévalo, 2008; Pedrera et al., 2020), joint gravity and thermal analysis (Carballo et al., 2015; Torne et al., 2015), and ambient noise tomography profiles (Palomeras et al., 2017). Where data density was insufficient, the CRUST1.0 crustal model was used (Laske et al., 2014).

To consider a realistic distribution of blocks in the uppermost part of the model, we use geological and tectonic maps of the study area (Marín-Lechado et al., 2017; Fernàndez et al., 2019; Clariana-García et al., 2021; Martín-Serrano et al., 2021; Matas & Martín-Parra, 2021a; Matas & Martín-Parra, 2021b; Montes et al., 2021; Roldán et al., 2021; IGME, 2021). This procedure permits the inclusion of small bodies that may affect the location of the shallowest earthquakes (e.g.: sedimentary basins).The summary of these data used to build mTAB3D is available in Table S1.

Using the intersections and depth relations between those surfaces, we can model the geometry of the main blocks following the same approach as Sánchez-Roldán et al. (2021). For instance, we defined the sedimentary cover by subtracting the topography (or bathymetry) from the basement top, and the basement is the volume within the basement top and the Moho discontinuity. Everything above the topography/bathymetry will be air/water, while the mantle will be below the modeled Moho surface. In addition, studies that identify changes in lithology or geophysical properties (e.g.: Gómez de la Peña et al., 2018) allow us to subdivide the area into different types of crust or crustal domains (i.e.: Iberian crust to the north, magmatic arc crust below the EAB, or oceanic crust in the easternmost part of the model).

We estimated the P-wave velocity of every type of block at each depth of the model according to relations that consider rock properties, such as composition and density (i.e.: Christensen & Mooney, 1995; Brocher, 2005) (Fig. S1A). We compared our estimations with previous results obtained in other studies of the region (i.e.: Grevemeyer et al., 2015; Mancilla & Díaz, 2015). This procedure has two exceptions: velocities above topography/bathymetry, and mantle blocks. We assigned a constant velocity of 1.5 km/s to those blocks that are above topography/bathymetry. On the other hand, we estimated the mantle velocity interpolating from a linear regression of the mantle velocity estimated in the ak135-F modified after Montagner and Kennet (1995), and since that is a 1D average model, we do not account for the lateral heterogeneity in the mantle (Fig. S1b).

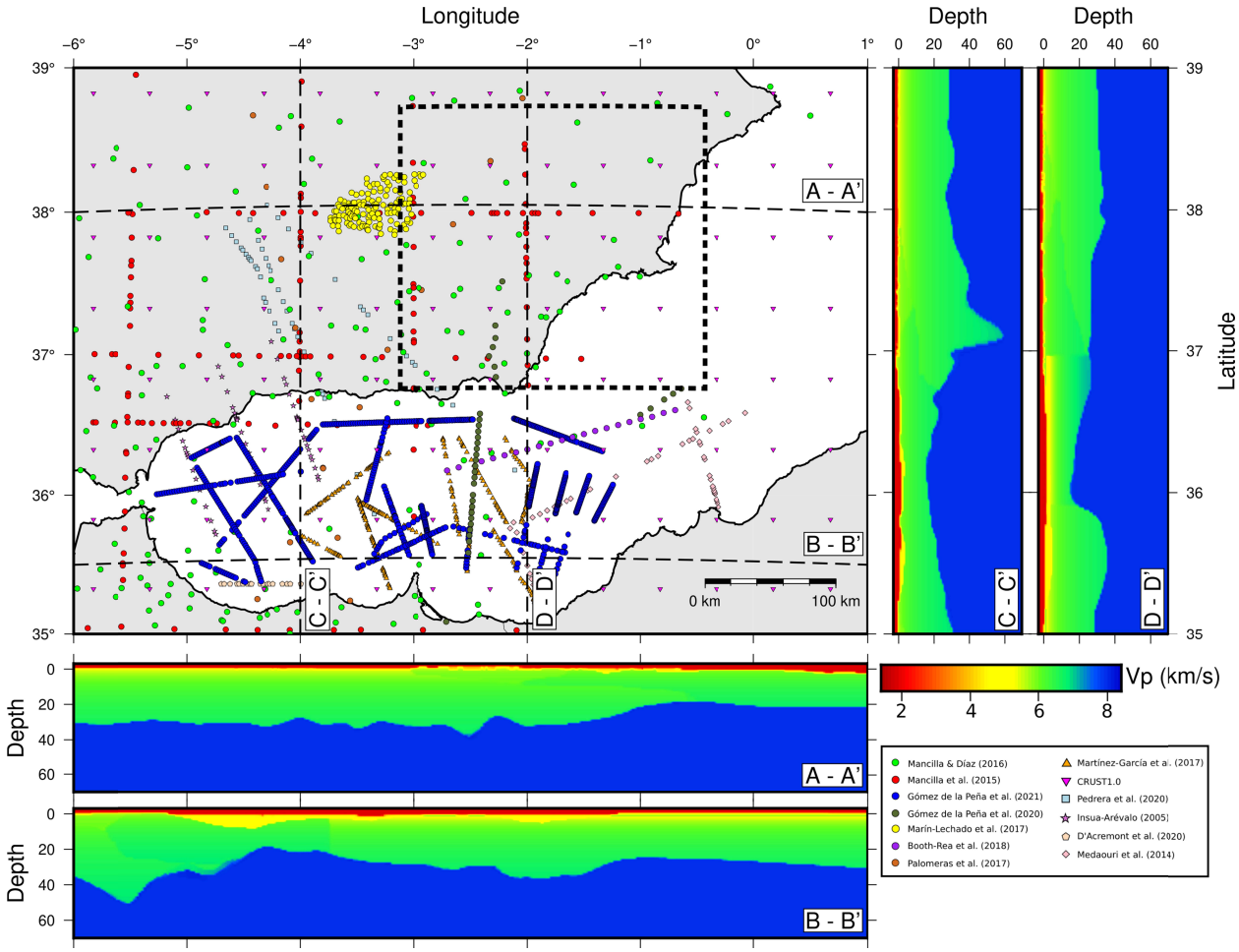

Figure 2

The main features in the mTAB3D velocity model (Fig. 2), are the distribution and relation among the different tectonic domains of the study area. For example, we modeled the progressive eastwards thinning of Iberia (A-A' section in Fig. 2) or the break-off of the sub-Iberian (C-C' section in Fig.2) and Maghrebian (D-D' section in Fig 2.) subducted lithosphere under the Eastern Betics (SE Iberia) and the Rif (northern Africa), respectively. Also, we accounted for some areas in the Alboran Sea where sedimentary subbasins and basement outcrops made contact (B-B' section in Fig. 2), which may be related to the presence of active faults of the TASZ (e.g.: WAB and SAB limited by the Al-Idrisi fault, see Fig. 1). Lastly, from this 3D layered distribution of blocks, we extract a grid with a maximum extent of 607x443x204 km^3, and with nodes every 1x1x1 km^3 where we assign a specific P-wave velocity value.

3.2 Earthquake absolute location computation

To test the performance of the mTAB3D velocity model, we computed a relocation using a dataset of 1598 earthquakes detected in the EBSZ between 2018-2022. Those results were compared to the obtained after relocating the same dataset using the 1D velocity model from

Mezcua and Martínez-Solares (1983) used in the Spanish Seismic Network for routine earthquake location, hereinafter, mIGN1D.

We retrieve arrival times recorded by the Spanish Seismic Network within the area covered by the 3D velocity model (Fig. S2; IGN, 2020). Then, we use the Nonlinloc software suite (NLL henceforth; Lomax et al., 2000). This software uses a non-linear location procedure which provides a statistically optimal solution and a posterior uncertainty estimation, expressed as the probability density function (PDF), and allows the use of a 3D velocity model. First, within the NLL suite, following a finite-differences, eikonal-equation algorithm (Podvin & Lecomte, 1991), we compute the theoretical travel-times with the Grid2Time program. Then, for the NLLoc program run, we adopted the equal differential-time (EDT) likelihood function in the procedure (Zhou, 1994; Font et al., 2004), which is more robust where outliers are present in the data. The Oct-Tree sampling algorithm (Lomax et al., 2000) estimates efficiently the maximum likelihood hypocenter of the PDF, which will be the preferred solution in this work. The NLLoc program allows us to calculate the 68% confidence ellipsoid from the PDF's, and thus we obtain the horizontal and vertical uncertainties (errH and errZ, respectively) based on the axes of this ellipsoid. Finally, after a first relocation, NLLoc estimates the average phase residuals in every station, which may act as station corrections for a second run of NLLoc over the dataset to compute more constrained solutions. This will be useful to reduce the contribution of any bias in the relocation process. It should be noted that in this procedure we will keep the same software, configuration parameters, and arrival times.

We set another test to know if this model could be suitable to study past seismic sequences within a specific zone and limited duration. For that, we chose the Al-Hoceima 2016 seismic sequence with 540 earthquakes of M≥2.5, registered by the Spanish Seismic Network on 2016-01-21 and 2016-04-01 in the TASZ. The geographical location of this sequence allows us to study the results that we should expect when relocating within an area close to the edge of our model, which implies fewer arrival times in the computing procedure and could bias the hypocenters. Here, we will also face the problem related to the distance to closer stations and their spatial distribution, which affects the quality of the solution, especially when assessing the hypocenter depth (Lomax et al., 2014).

In this scenario, we perform an additional procedure to the relocation in NLL, similar to the one explained in Lomax and Savvaidis (2022), which consists in computing the source-specific station term corrections (SSST) during the hypocentral relocation procedure using the program Loc2SSST within the Nonlinloc suite. These SSSTs fluctuate in the 3D velocity model and, during the iterative operation, the program generates specific files for every station and phase that contain the time correction value at each node of the model. Despite the computational cost of this method, the advantage of this procedure lies in the possibility of running several instances of Loc2SSST in parallel, which improves the time performance during runtime. Besides, it offers stable and reliable hypocenters in a situation with fewer available stations in the vicinity of the seismic sequence.

4 Results

4.1 EBSZ 2018-2022 catalog

The compiled catalog comprises 1598 earthquakes detected by the Spanish Seismic Network (IGN, 2022), with magnitudes ranging from 0.4-4.1, recorded between 2018-2022 in

the southeastermost part of the Iberian peninsula. We have relocated all the events using two different velocity models, the mTAB3D and the mIGN1D. We chose this spatiotemporal window because this geographic area is prone to diffuse seismicity with casual seismic sequences, such as the one that occurred in the Albudeite and Mula towns in 2018 (Fig. 3), with an Mw 4.1 mainshock.

Since mTAB3D only accounts for P-wave velocity, we applied a local constant V_P/V_S ratio of 1.73, obtained after plotting tS-tP arrival times at each station against tP absolute arrival times in a Wadati diagram (Fig. S3a). This V_P/V_S ratio is consistent with the value proposed in receiver function studies that use stations within our study area (Mancilla et al., 2015b).

The comparison of the hypocenter location between mIGN1D (Fig. 3a) and mTAB3D (Fig. 3b) shows subtle differences; however, we can observe some particularities. The first one is related to the depth distribution of hypocenters; in both cases, seismicity seldom exceeds 15 km in depth. Nevertheless, the percentage of hypocenters that converge around 0 km in mIGN1D nearly doubles the amount relocated by mTAB3D (Fig. 3).

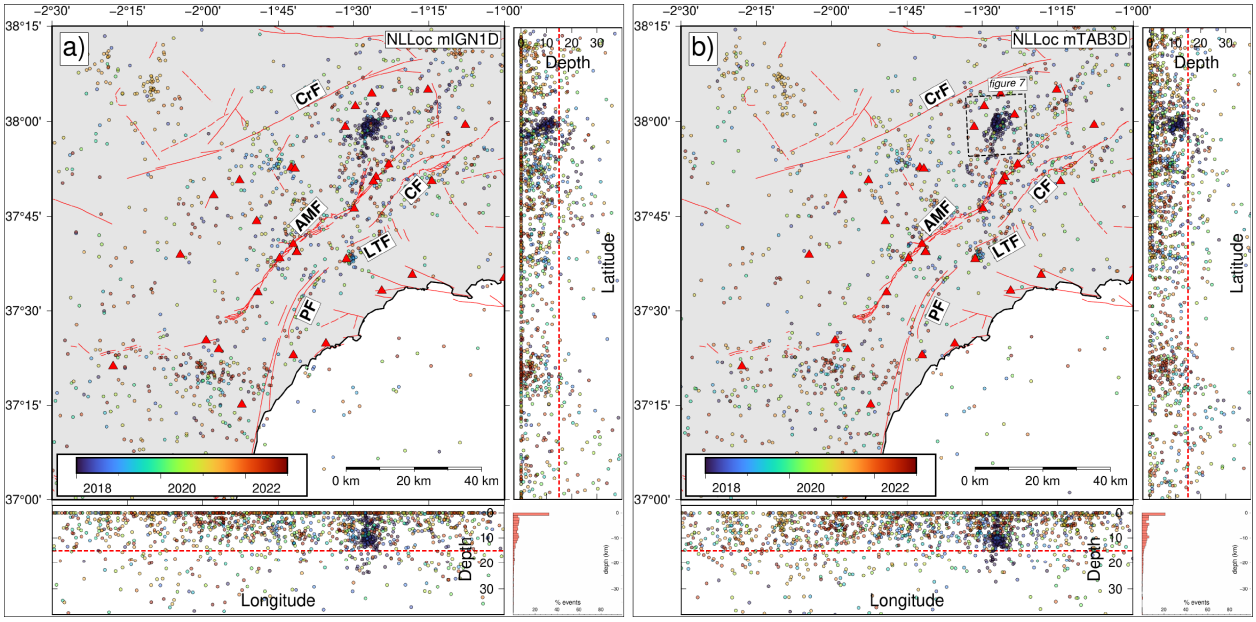

Figure 3

Secondly, if we focus on epicentral distribution, hypocenters obtained with mTAB3D are slightly closer to the nearest faults (e.g.: PF, AMF, CF) (Fig. S4). In addition, mTAB3D gets a better clustering of the events in some areas, such as the LTF. After normalizing the number of epicenters per unit of area (Fig. 4), in this case, 10 km^2, we obtain the main clusters after the relocation. Results are similar between mTAB3D and mIGN1D in terms of events distribution, although mIGN1D gets two small clusters to the west of PF in an area where mTAB3D does not achieve enough density. However, the foremost difference lies in the evident cluster localized to the NE of the interest area, where most of the epicenters are related to a seismic sequence that occurred in 2018 between CrF and AMF. Here, epicenter density is much higher after relocating with mTAB3D.

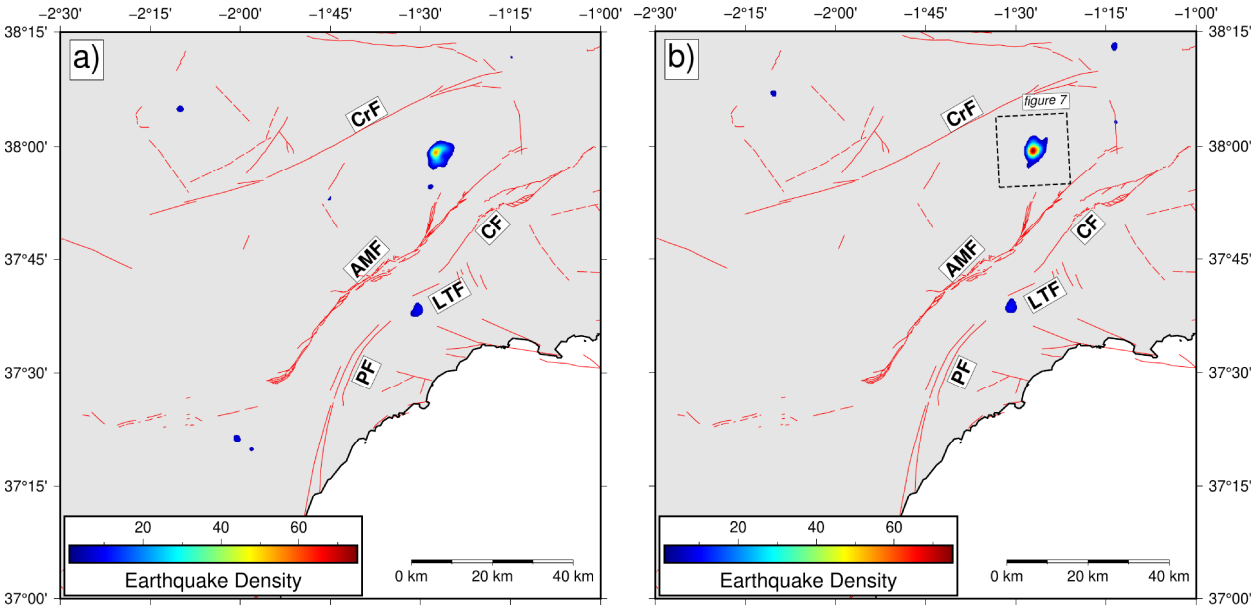

Figure 4

293

294 4.2 Al-Hoceima 2016 seismic sequence

295 The Al-Hoiceima series (2016) starts with an Mw 5.0 foreshock on 2016-01-21 in the
296 South Alboran Sea, followed by an Mw 6.3 mainshock that occurred on 2016-01-25 (Buforn et
297 al., 2017). This earthquake was highly felt in Al-Hoceima (northern Morocco) and other nearby
298 cities causing several injuries and damaging buildings and infrastructures. At large distances,
299 such as in southern Iberia, people felt it with intensity IV (IGN, 2016). The sequence comprises
300 >2400 earthquakes until June 2016, but we selected a subset of 540 earthquakes with M≥2.5
301 detected by the Spanish Seismic Network between January 21st 2016 and April 1st 2016, the
302 period of the main activity. Following the same method used in the analysis of the EBSZ 2018-
303 2022 catalog, we obtained a VP/VS ratio of 1.74 (Fig. S3b). For this relocation of the catalog, we
304 proceeded similarly to the workflow explained in Lomax & Savvaidis (2022) for the NLL-SSST
305 hypocenter inversion. Table 1 shows the parameters to specify the criteria for the event location
306 in every iteration of the procedure. The weighted mean of rms was calculated repeatedly
307 considering the previous parameters and a shrinking spatial smoothing, D, starting at 4 km and
308 finishing at 1 km after the last run.

Table 1

rms	**no. readings**	**gap**	**P-arrival rms**	**S-arrival rms**	**len3**
1.0 s	25	180º	1.0 s	2.0 s	10.0 km

309

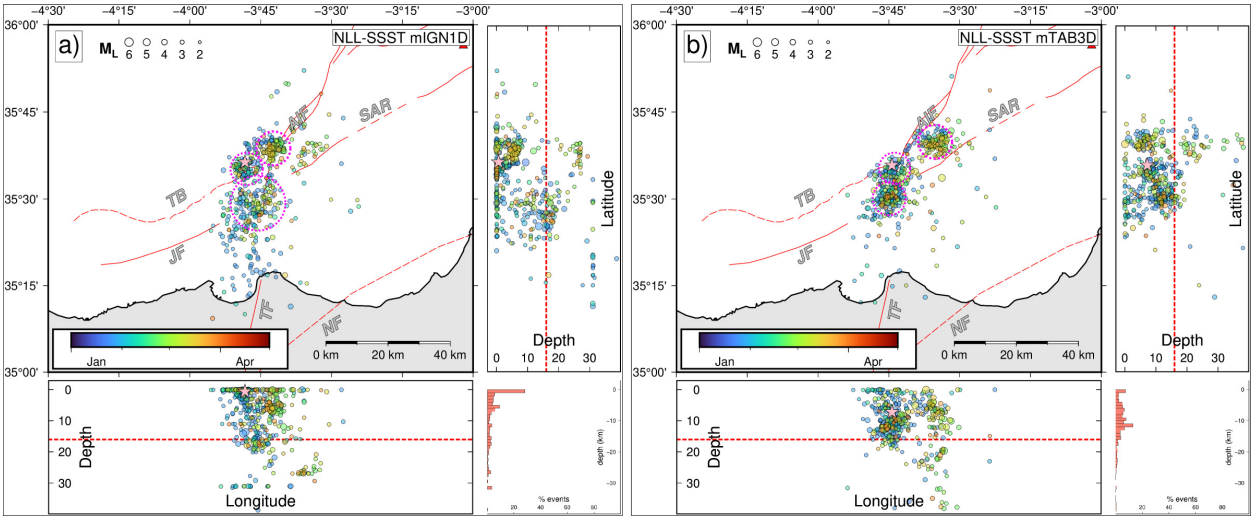

Figure 5

310

311 The absolute locations of the seismic sequence following the NLL-SSST procedure show
312 that most of the epicenters tend to shift eastwards, close to the AIF area, in contrast with
313 mIGN1D, which keeps the seismicity westwards from the traces of the main faults (Fig. 5).
314 Regarding the depth distribution, our results indicate that seismicity ranges mostly from 0 km to
315 16 km and drastically decreases below this point. This is not observed in the mIGN1D results
316 because many hypocenters converge around 0 km. The southernmost hypocenters computed with
317 this 1D velocity model are systematically located at 30 km, which does not happen in the
318 mTAB3D results (Fig. 5).

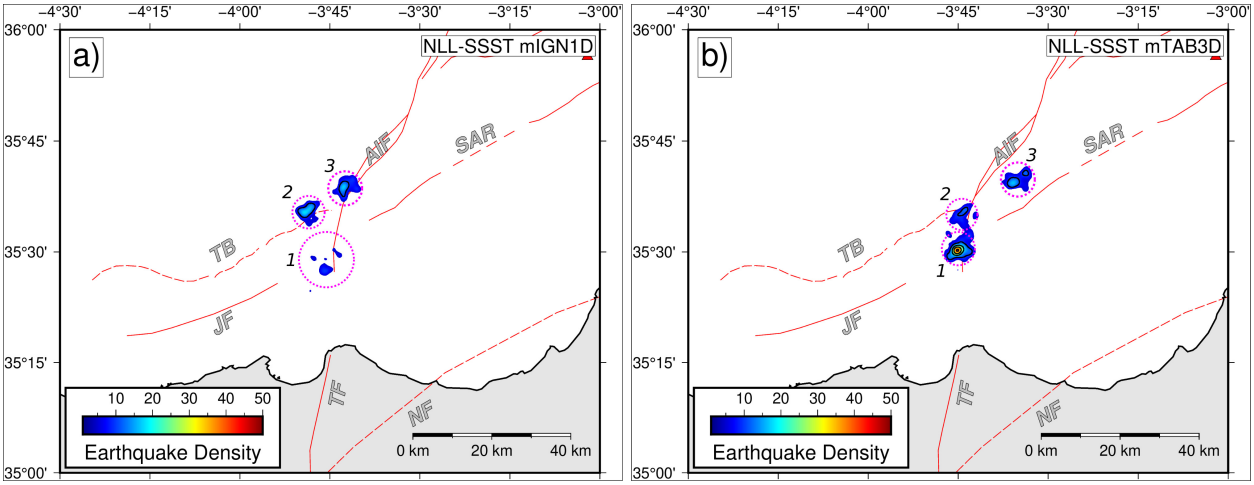

Figure 6

319

320 Both relocations have three main clusters (Figs. 5 & 6), but there are differences in their
321 distribution and density. For example, epicenters obtained using the mIGN1D show a sparse
322 distribution of seismicity when compared with the results using the mTAB3D, which achieves a
323 higher density of hypocenters (Fig. 6). The northern cluster (number 3 in Fig. 6) that occurs
324 around March is mainly located on the trace of AIF, while the same seismicity shifts to the east,

between AIF and South Alboran Ridge (SAR), when localized with the mTAB3D (Figs. 5 & 6). The southernmost cluster's area (number 1 in Fig. 6) extends beyond the JF surface trace in mIGN1D results, in contrast, the results obtained with mTAB3D show that the same earthquakes are mostly confined to the northwest of the fault trace (Figs. 5 & 6). Regarding the depth distribution of the clusters, mTAB3D located these three clusters progressively deeper from north to south (latitude depth cross section in Fig. 5b).

5 Discussion

As described in the previous section, the results of the hypocentral relocation vary greatly depending on the velocity model used. However, we need to understand how reliable the absolute locations from each model are. For this purpose, we used the covariance matrix calculated by Nonlinloc from the PDF obtained in the relocation. From this covariance matrix, we computed the vertical uncertainty (errZ) and a horizontal uncertainty ellipse, both with a 68 % confidence level. From this ellipse, the horizontal uncertainty (errH) is assessed after calculating the geometric mean between the horizontal semi-minor and semi-major axes. Both vertical and horizontal values are given in kilometers.

5.1 Uncertainty analysis of a continuous catalog in the EBSZ

In the case concerning the absolute location of a catalog in the area of EBSZ between 2018-2022, we divided the results into four levels of quality according to the number of arrivals used during the inversion for each hypocenter (A: Num. arrivals ≥ 40; B: 20 ≤ Num. arrivals ≤ 40; C: 10 ≤ Num. arrivals ≤ 20; D: Num. Arrivals < 10).

Table 2

	Q_A = 63		**Q_B = 253**		**Q_C = 620**		**Q_D = 662**	
	errH	*errZ*	*errH*	*errZ*	*errH*	*errZ*	*errH*	*errZ*
mIGN1D	0.99	1.10	1.36	1.58	1.99	2.62	15.37	11.11
mTAB3D	0.94	1.32	1.28	1.92	1.79	2.63	13.67	9.81

The calculated average horizontal uncertainty (errH) for the four subsets (A to D) is always lower in mTAB3D than in mIGN1D (Table 1). Nevertheless, the mIGN1D performs better than the mTAB3D vertical error (errZ) except for the lowest quality subset.

It is worth noting that, even though mIGN1D's depth solutions may seem more reliable in general, we found that the number of hypocenters that converges at 0 km double the mTAB3D catalog (histograms in Fig. 3). In addition, mTAB3D achieves a lower errH and epicentral location tends to be closer to active structures in the area, at least for the main clusters (Fig. 4 and Fig. S4). Hypocenters computed with mIGN1D generally show worse constrained locations when confronted against the same earthquake located with mTAB3D, especially for those events relocated using few arrival times (Q_D subset in Table 2), which usually are related to low-magnitude earthquakes and involve the most common type of seismicity in the region of EBSZ. Comparing uncertainties earthquake by earthquake and plotting the results in a histogram, we see that mTAB3D solutions are more reliable on average (Fig. S5).

The observed dissimilarity between relocations obtained using both velocity models could be related to the over-simplification committed by the mIGN1D when considering the velocity structure of the EBSZ. This structural zone limits two different crust domains composed of geological units with contrasting properties (e.g.: sedimentary basins or volcanic rocks) (De

Larouzière et al., 1988) that could affect the wave propagation and, hence, influence the arrival times at stations (Thurber, 1992). Applying station corrections computed by Nonlinloc partially solves this issue for mIGN1D. Nevertheless, those corrections refer only to near-surface velocity variations under the stations (Husen and Hardebeck, 2010), which could be a drawback when relocating hypocenters within tectonically complex regions. In contrast, mTAB3D takes into account this complexity and, thus, the obtained location of the hypocenters may be more reliable to carry out the seismotectonic analyses in EBSZ. Seismicity in this area is mainly restricted to the first 12-15 km of crust (García-Mayordomo, 2005) and shows a scattered distribution (Stich et al., 2003); however, our results show that earthquakes and small seismic sequences are closer to faults that bound basement blocks and sedimentary basins. The Guadalentín Valley, for example, is bounded to the northwest by AMF and to the southeast by PF, LTF, and CF (Fig. 3). Different geological studies have identified some of these faults as the source for some of the most relevant seismic sequences both in the instrumental and historical records (López-Comino et al., 2012; Insua-Arévalo et al., 2015; Martín-Banda et al., 2021; Martínez-Díaz et al., 2012, 2018). The hypocenters computed with mTAB3D distinguish a small sequence close to the LTF and several epicenters along AMF and CF traces. This distribution is consistent with the hypothesis of greater earthquake density around rigid and fractured basement blocks, uplifted on the hanging wall of active faults (i.e.: CF, AMF, LTF). In contrast, the Guadalentín Valley, the basin area in between the active faults (Figs. 1 and 3), shows lower seismicity density probably due to its different rheological behavior (Rodríguez-Escudero et al., 2020; Alonso-Henar et al., 2021).

Concerning the earthquakes that are unlike to be caused by large-scale faults in the area and appear far from them, some studies deduce that these events, which can occur in any place, are triggered due to the high density of small-scale faults within the major tectonic blocks under a transpressional regime (Echeverria et al., 2013; Rodríguez-Escudero et al., 2014). For example, the 2018 seismic sequence in the Mula-Archena subbasin is located between the CrF and the AMF but apparently unrelated to a clear source (Fig. 4). Focusing on this sequence, we observe that the closest faults are Mula-Archena fault (MAF) and Tollos-Rodeos fault (TRF) (Fig. 7a). These NE-SW faults are assumed to dip steeply, and given their length, inferred from local cartography (Silva et al., 1996; Martínez-Díaz, 1999), they could reach the depth where the sequence occurs (~10-12 km). However, MAF and TRF orientation is not coherent with the cloud's shape, which infers a plane dipping northwards. The focal mechanism obtained from the moment tensor solution computed by the Spanish Seismic Network also shows E-W nodal plane dipping northwards, and the depth of the centroid is similar to the one of the denser clustering (Fig. 7b). There are minor E-W (N80ºE to N110ºE) subvertical faults in the area affecting the sedimentary cover (blue lines in Fig. 7a) and showing reverse and left-lateral strike-slip kinematics, which could act as possible linkages between major SE-NE faults (Martínez-Díaz, 1999). Although the behavior and geometry of these faults in depth are not well known, Herrero-Barbero et al. (2020), after the reinterpretation of seismic profiles in the area of the Mula-Archena subbasin, suggest the presence of some faults with highly dipping angles that would mainly affect pre-Messinian formations at the bottom of the basin. These faults are interpreted with normal kinematics, but they could have been reactivated as reverse faults under the transpressional regime that started in the late Miocene, as has also been inferred from the AMF activity (Meijninger and Vissers, 2006; Herrero-Barbero et al., 2020). In this situation, the basement units would be highly fractured due to a network of short-scale faults, which could also limit the maximum magnitude of an earthquake in a seismic sequence (Leonard, 2010). Thus,

these faults could accommodate part of the deformation in the area and eventually may trigger seismicity similar to the 2018 seismic sequence.

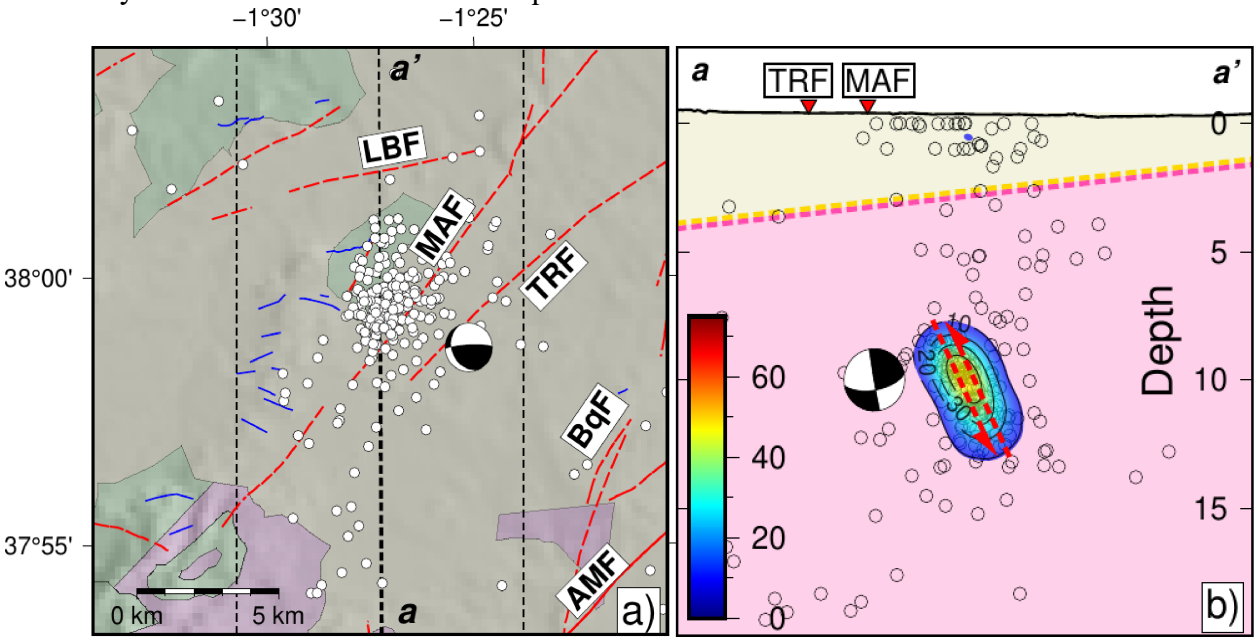

Figure 7

5.2 Uncertainty analysis of Al-Hoceima 2016 seismic sequence

This seismic sequence exemplifies how 1D velocity models may distort the findings, causing the epicenter to shift away from the inferred source fault (Thurber, 1992; Husen and Hardebeck, 2010). Epicenters computed with the mIGN1D velocity model following the NLL-SSST procedure are scattered and placed west of the AIF (Fig. 4), the fault that may have produced the event (Gràcia et al., 2019). Besides, there is a high percentage of hypocenters that converge around 0 km. This could suggest that this model does not resolve properly the uppermost velocities in the area and does not account for variations caused by geological units like sedimentary basins.

Regarding the reliability of the results obtained using mTAB3D, we got the values of the 68% confidence ellipsoid to represent the uncertainty of the hypocentral location (Table 3), as previously described for the continuous catalog of EBSZ. Due to the lower number of stations around the area where the Al-Hoceima 2016 seismic sequence occurred (some of the broadband stations and accelerometers were deployed after the sequence), we modified the quality criteria to divide the catalog into different subsets (A: No. arrivals $\geq$ 30; B: 20 $\leq$ No. arrivals $\leq$ 30; C: 15 $\leq$ No. arrivals $\leq$ 20; D: No. arrivals < 15). This time, the comparison of the uncertainties shows that mTAB3D achieves more reliable locations given the lower values for both errH and errZ in every quality subset (Table 3, Fig. S6). So, since mTAB3D shows better constrained hypocenters and improves the clustering among events, even in this situation of high azimuthal gap and large distances to the seismic stations, we decided to use these results to analyze the seismic sequence within the complex tectonic setting of the Alboran basin.

Table 3

	Q_A = 78		Q_B = 262		Q_C = 101		Q_D = 99	
	errH	*errZ*	*errH*	*errZ*	*errH*	*errZ*	*errH*	*errZ*
mIGN1D	4.71	9.94	5.60	12.64	6.75	15.61	10.13	18.03
mTAB3D	3.99	9.87	4.09	10.89	4.99	13.13	7.26	15.38

Our results suggest that the Mw 6.3 mainquake of this sequence occurred slightly south to a right-stepping bend of the AIF (Fig. 5). After a finite source modeling, Stich et al. (2020) observe that the rupture propagates asymmetrically from the nucleation zone: southwards, following the fault trace (N10ºE), with a maximum length of ~8 km (which is similar to the distance to the southernmost cluster after our relocation); northwards, the rupture is ~13 km following the orientation of the double restraining belt (N40ºE). Here, we also found some relocated aftershocks aligned between the two branches of the restraining bend. Several studies show how intricate geometries could influence earthquake rupture (i.e.: Oglesby & May, 2012; Howarth et al., 2021). Compressive step-overs may act as barriers impeding the rupture propagation (Elliot, et al., 2015). However, the rupture can go further when the stress drops drastically, in our case, at the northeasternmost end of the primary fault segment where the rupture nucleates (Oglesby, 2008), inducing a stress increase and nucleation of the rupture in the N40ºE strand of AIF, which may be the case for the Mw 6.3 mainquake, as we could infer from the slip distribution scenarios from Stich et al. (2020).

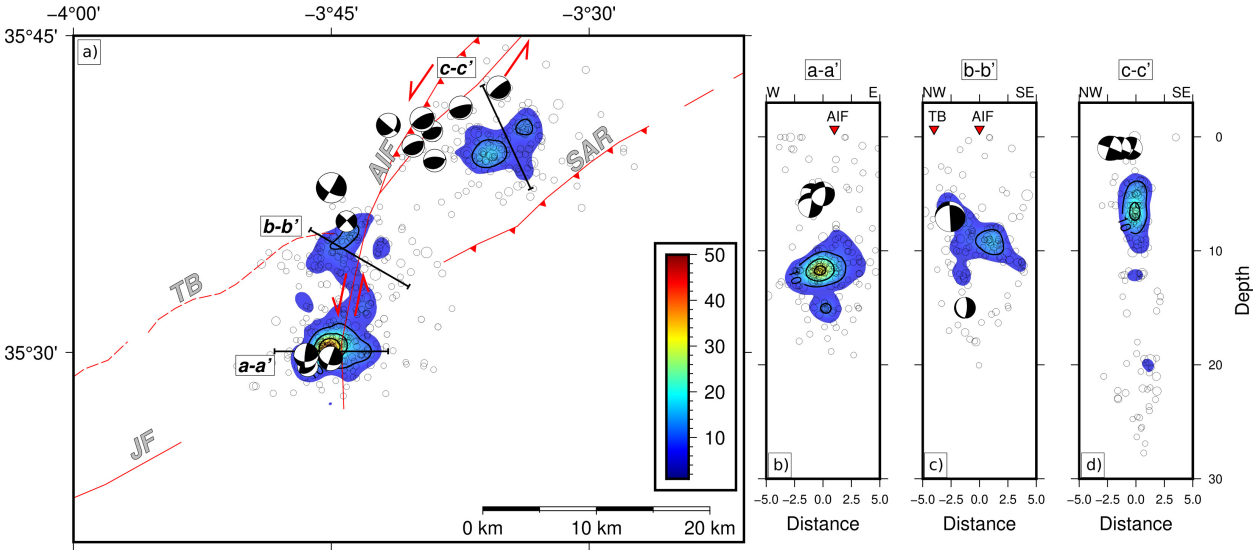

Figure 8

As previously explained, the seismicity related to this sequence appears to be grouped into three main clusters (Figs. 5 and 8a). Two of those clusters follow AIF's trace but finish abruptly where this fault intersects the TB (Fig. 8b and 8c). In this area, Gràcia et al. (2019) interpreted the presence of flower structures with folds and minor sub-vertical faults that converge in depth, and proposed that the structure may be related to the regional transpressional kinematic setting. On the other hand, in the area between AIF and SAR (Fig. 8d), where the other cluster lies, Gràcia et al. (2019) describe folds and reverse faults. Additionally, the focal mechanisms computed by Buforn et al. (2017) can be grouped into two sets of kinematics depending on the area: those dominated by strike-slip component are more frequent in the

clusters on the AIF trace (Figs. 8a-c), whereas those showing reverse faulting are more common in the western tip of the Alboran Ridge, close to the other epicenter grouping (Figs. 8a and 8d).

This difference in the structures observed in the subsurface and how the dominant kinematics varies between zones support the idea of slip partitioning as the main controlling factor for the evolution of this sequence (Gràcia et al., 2019; Stich et al., 2020). In this case, seismicity starts in the Al-Idrisi fault zone, where its left-lateral slip accommodates part of the deformation. Stress transfer to the NE could reactivate faults in the area of SAR, triggering a sequence of aftershocks where thrusting is the most common mechanism due to the favorable orientation of those reverse faults according to the regional shortening (Serpelloni et al., 2007; Martínez-García et al., 2017). After the relocation, we achieved better clustering around those regions, even discriminating between two subsets in the Al-Idrisi fault zone. The average depth of those clusters does not exceed 15 km (Figs. 5b-d), which is in accordance with the crustal thickness estimates obtained from geophysical studies (i.e.: Palomeras et al., 2017; Gómez de la Peña et al., 2018) that image a fairly thin crust where the seismogenic zone would be constrained in the first 20 km (Grevemeyer et al., 2015; Gómez de la Peña et al., 2022).

5.3 Limiting factors and future work to consider after the location procedure

We have presented two examples of relocations carried out in different scenarios. In the first one, we have a nearly ideal case where the stations are evenly distributed, in addition to not being so far from the areas of seismic activity (Fig. 3). Under these circumstances, the type of velocity model (1D vs. 3D) seems to act as a remarkable factor only when referring to the location errors of the events classified in the low-quality dataset, as we have shown previously (Table 2). However, it is interesting to consider the lateral variation of P-wave velocity when we study areas where active structures occur as boundaries between highly contrasting lithologies, and hence, different physical properties that may affect the wave propagation. Although station delays partly compensate for this effect when we computed the relocation with a 1D model, sometimes it is not enough to rely only on the seismic network quality if we try to establish which zones show higher activity or when we need to avoid biased locations. In these situations, 3D models could help us to obtain constrained solutions.

In the second relocation, the seismicity appears confined to an area close to the southernmost boundary of mTAB3D. Due to the unfavorable distribution of stations for this sequence, we observe that the accuracy obtained by mIGN1D and mTAB3D is worse, especially for the vertical uncertainty (Table 3). However, we noted that choosing between 1D or 3D models could imply an important decision that may affect our results even in this adverse setting (Figure S7 in Supplementary Material). Waves traveling longer distances could propagate across different units that somewhat influence their path, leading to higher uncertainties. The Al-Hoceima sequence illustrates how we may reduce possible biased solutions when the velocity model comprises important boundaries, such as the Al-Idrisi fault between two crustal domains.

Although mTAB3D shows how 3D velocity models improve the hypocenter location in complex tectonic areas, there are other fields where these models may be applied. For example, physics-based simulations include 3D velocity models in the workflow for computing ground motion predictions (Bradley, 2019; De la Puente et al., 2020). The historical and instrumental catalogs demonstrate that the westernmost Mediterranean is prone to damaging earthquakes, and mTAB3D may become an additional tool for obtaining ground-shaking maps, which are crucial for seismic hazard analysis and engineering studies. Lastly, the number and frequency of works

carried out in our study area allow us to incorporate more data into this model to enhance its resolution and quality.

5 Conclusions

Reliable earthquake absolute locations are crucial for seismotectonic studies in complex tectonic areas. The westernmost Mediterranean region, due to its complicated geological history, includes domains with variable geometries and properties that may affect wave propagation once an earthquake occurs. In this context, we gathered data from previous studies at local and regional scales to build a P-wave velocity model (mTAB3D) consisting of a 3D grid that accounts for the lateral heterogeneity in our study area. Our model is divided into several blocks to represent the most characteristic bodies in the region (air/water, sedimentary basins, basements of different natures, and upper mantle). Despite the presence of areas, usually situated at the edges of the grid, where the scarcity or low resolution of data sources could produce a priori uncertainties in the resolved geometries, we are confident that the mTAB3D is reliable and realistic enough to reflect significant features such as the crustal thinning in the West Alboran Basin, and the structures that bound various crustal domains, both onshore and offshore.

We tested the performance of this model by relocating two seismic catalogs: the first is a continuous dataset recorded between 2018-2022 in the EBSZ, and the second comprises arrival times recorded during the Al-Hoceima seismic sequence in 2016. We compared each relocation against a catalog built after relocating with a 1D velocity model (mIGN1D) using the same dataset and following the same procedure. For the EBSZ catalog, we observed lower uncertainties in mTAB3D than in mIGN1D when resolving the epicentral location. The difference between results is especially emphasized when comparing errH and errZ in the subsets of low-magnitude earthquakes recorded by a few stations. In the case of the Al-Hoceima sequence, we applied the recent NLL-SSST method (Lomax & Savvaidis, 2022) and, although hypocenters lie close to the southernmost border where the wider azimuthal gap may influence the reliability, mTAB3D achieved the lowest uncertainty in every subset of quality and allowed us to discriminate different clusters. In both catalogs, the new hypocenters correlate reasonably well with the active faults present in both studied areas or enhance the seismic clusters.

Accordingly, mTAB3D may provide stronger hypocentral locations that may result in a quality improvement for seismotectonic studies. Finally, although we applied this model to recent seismicity, it can be valuable for studies focused on prior series where poorly constrained velocity models lead to unfavorable or biased locations. This methodology may be implemented when re-interpreting some past earthquakes and, thus, to a better understanding of southern Iberia and the westernmost Mediterranean seismogenic processes.

Acknowledgments

This manuscript was significantly enhanced by helpful comments from [...]. The authors declare no competing interests. This research was supported by grant STRENGTH (PID2019-104668RB-I00) funded by MCIN/AEI/10.13039/501100011033 and grant Model_SHaKER (PID2021-124155NB-C31) funded by MCIN/AEI/10.13039/501100011033 and by the "European Union NextGenerationEU/PRTR". The author JLSR owns a predoctoral research grant (FPI ref. PRE2018-083913) funded by MCIN/AEI/10.13039/501100011033 and by "ESF Investing in your future".

Open Research

Earthquake phase arrival seismic stations dataset was accessed through the Spanish Seismic Network (https://www.ign.es/web/ign/portal/sis-catalogo-terremotos). Focal mechanisms were obtained from the Spanish Seismic Network seismic moment tensor catalog (https://www.ign.es/web/ign/portal/tensor-momento-sismico/-/tensor-momento-sismico/getExplotacion, last accessed December 2022). Main active faults traces are from QAFI v.4. (http://info.igme.es/qafi/, last accessed December 2022). Geophysical Information System available from Instituto Geológico y Minero (IGME) avalilable at http://info.igme.es/SIGEOF/ (last accessed December 2017). Nonlinloc software can be accessed through its GitHub repository (https://github.com/alomax/NonLinLoc). Figures and maps were built using the Generic Mapping Tools software (Wessel et al., 2019). This manuscript was written using LibreOffice Writer (https://www.libreoffice.org, last accessed February 2023). Supplementary material for this article includes tables and text with the summary of data used and the procedure to build mTAB3D. Raw grid files and metadata of mTAB3D model in under internal review for being released in a public repository.

References

Alfaro, P., Delgado, J., Sanz de Galdeano, C., Galindo-Zaldívar, J., García-Tortosa, F. J., López-Garrido, A. C., López-Casado, C., Marín-Lechado, C., Gil, A., & Borque, M. J. (2008). The Baza Fault: a major active extensional fault in the central Betic Cordillera (south Spain). *Int J Earth Sci (Geol Rundsch), 97*, 1353–1365. https://doi.org/10.1007/s00531-007-0213-z

Alonso-Henar, J., Rodríguez-Escudero, E., Herrero-Barbero, P., Tsige, M., & Martínez-Díaz, J. J. (2021). Complete strain record of a highly asymmetric shear zone: from fault core gouges to surface rupture of historical earthquakes in the Alhama de Murcia Fault (SE Iberian Peninsula). *Lithosphere*, *2021*(1). https://doi.org/10.2113/2021/8876012

Amante, C. & B.W. Eakins, 2009. ETOPO1 1 Arc-Minute Global Relief Model: Procedures, Data Sources and Analysis. NOAA Technical Memorandum NESDIS NGDC-24. National Geophysical Data Center, NOAA (last accessed December 2022). https://doi.org/10.7289/V5C8276M

Ammar, A., Mauffret, A., Gorini, C., & Jabour, H. (2007). The tectonic structure of the Alboran Margin of Morocco. *Rev. Soc. Geológica Esp.*, *20*(3-4). 247-271.

Amores Lahidalga, R., Hernández-Enrile, J. L., & Martínez-Díaz, J. J. (2002). Estudio gravimétrico previo aplicado a la identificación de fallas ocultas como fuentes sismogenéticas en la Depresión de Guadalentín (Región de Murcia). *Geogaceta, 32*(1), 307-310 (in Spanish).

Argus, D. F., Gordon, R. G., & DeMets, C. (2011). Geologically current motion of 56 plates relative to the no-net-rotation reference frame: NNR-MORVEL56. *Geochem., Geophys., Geosys., 12*(11), 1-13. https://doi.org/10.1029/2011GC003751

Arroucau, P., Custódio, S., Civiero, C., Silveira, G., Dias, N., Díaz, J., Villaseñor, A., & Bodin, T. (2021). PRISM3D: a 3-D reference seismic model for Iberia and adjacent areas. *Geophysical Journal International, 225*(2), 789–810. https://doi.org/10.1093/gji/ggab005

Balanyá, J. C., & García-Dueñas, V. (1987). Les directions structurales dans le Domaine d'Alborán de part et d'autre du Détroit de Gibraltar. *C. R. Acad. Sci., Ser. II, 304*, 929– 932.

583 Ballesteros, M., Rivera, J., Muñoz, A., Muñoz-Martín, A., Acosta, J., Carbó, A. &
584 Uchupi, E. (2008) Alboran basin, Southern Spain. Part II: Neogene tectonic implications for the
585 orogenic float model. *Mar. Petrol. Geol., 25*, 75– 101.
586 https://doi.org/10.1016/j.marpetgeo.2007.05.004

587 Biggs, J., Bergamn, E., Emmerson, B., Funning, G., Jackson, J., Parsons, B., & Wright,
588 T. (2006). Fault identification for buried strike-slip earthquakes using InSAR: the 1994 and 2004
589 Al Hoceima, Morocco earthquakes. *Geophys. J. Int., 166*, 1347-1362.
590 https://doi.org/10.1111/j.1365-246X.2006.03071.x

591 Booth-Rea, G., Ranero, C. R., Martínez-Martínez, J. M., & Grevemeyer, I. (2007).
592 Crustal types and Tertiary tectonic evolution of the Alborán sea, western Mediterranean.
593 *Geochem., Geophys., Geosys. 8*(10). https://doi.org/10.1029/2007gc001639

594 Booth-Rea, G., Martínez-Martínez, J. M., & Giaconia, F. (2015). Continental subduction,
595 intracurstal shortening, and coeval upper-crustal extension: P-T evolution of subducted south
596 Iberian paleomargin metapelites (Betics, SE Spain). *Tectonophysics, 663*, 122-139.
597 https://doi.org/10.1016/j.tecto.2015.08.036

598 Booth-Rea, G., Ranero, C. R., & Grevemeyer, I. (2018). The Alboran volcanic-arc
599 modulated the Messinian faunal exchange and salinity crisis. *Sci. Rep.,* 8.
600 https://doi.org/10.1038/s41598-018-31307-7

601 Borque, M. J., Sánchez-Alzola, A., Martín-Rojas, I., Alfaro, P., Molina, S., Rosa-Cintas,
602 S., Rodríguez-Caderot, G., de Lacy, C., García-Armenteros, A., Avilés, M., Herrera-Olmo, A.,
603 García-Tortosa, F. J., Estévez, A., & Gil, A. J. (2019). How much Nubia-Eurasia convergence is
604 accommodated by the NE end of the Eastern Betic Shear Zone (SE Spain)? Constraints from
605 GPS velocities. *Tectonics, 38*(5), 1824– 1839. https://doi.org/10.1029/2018TC004970

606 Bourgois, J., Mauffret, A., Ammar, A., & Demnati, A. (1992). Multichannel seismic data
607 imaging of inversion tectonics of the Alboran Ridge (western Mediterranean Sea). *Geo-Marine*
608 *Letters, 12*(2-3), 117-122. https://doi.org/10.1007/BF02084921

609 Bousquet, J. C. (1979). Quaternary Strike-Slip Faults in Southeastern Spain.
610 *Developments in Geotectonics, 13.* 277-286. https://doi.org/10.1016/B978-0-444-41783-
611 1.50044-1

612 Bousquet, J. C., & Philip H. (1976). Observations Microtectoniques Sur La Compression
613 Nord-Sud Quaternaire Des Cordilleres Betiques Orientales (Espagne Meridionale-Arc de
614 Gibraltar). *Bull. Soc. Géol. France, 7*(3), 711-724 (in French).

615 Bouyabaouene, M. L., Goffé, B., & Michard, A. (1995), High-pressure, low-temperature
616 metamorphism in the Sebtides nappes, northern Rif, Morocco, *Geogaceta, 17*, 117– 119.

617 Bradley, B. A. (2019). On-going challenges in physics-based ground motion prediction
618 and insights from the 2010–2011 Canterbury and 2016 Kaikoura, New Zealand earthquakes. *Soil*
619 *Dynamics and Earthquake Engineering, 124*, 354-364.
620 https://doi.org/10.1016/j.soildyn.2018.04.042

621 Brocher, T. M. (2005). Empirical relations between elastic wavespeeds and density in the
622 Earth's Crust. Bull. *Seismol. Soc. Am., 95*(6), 2081-2092. https://doi.org/10.1785/0120050077

Buforn, E., Pro, C., Sanz de Galdeano, C., Cantavella, J. V., Cesca, S., Caldeira, B., Udías, A., & Mattesini, M. (2017). The 2016 south Alboran earthquake (Mw=6.4): A reactivation of the Ibero-Maghrebian region? *Tectonophysics, 712-713*, 704-715. https://doi.org/10.1016/j.tecto.2017.06.033

Calvert, A., Sandvol, E., Seber, D., Barazangi, M., Roecker, S., Mourabit, T., Vidal, F., Alguacil, G., & Jabour, N. (2000). Geodynamic evolution of the lithosphere and upper mantle beneath of Alboran region of the western Mediterranean: Constraints from travel time tomography. *Journal of Geophysical Research: Solid Earth, 105*, 10871-10898. https://doi.org/10.1029/2000JB900024

Carannante, S., Argnani, A., Massa, M., D'Alema, E., Lovati, S., Moretti, M., Cattaneo, M., & Augliera, P. (2015). The May 20 (Mw 6.1) and 29 (Mw 6.0), 2021, Emilia (Po Plain, northern Italy) earthquakes: New seismotectonic implications from subsurface geology and high-quality hypocenter location. *Tectonophysics, 665*, 107-123. https://doi.org/10.1016/j.tecto.2015.05.015

Carballo, A., Fernandez, M., Jiménez-Munt, I., Torne, M., Vergés, J., Melchiorre, M., Pedreira, D., Afonso, J. C., García-Castellanos, D., Díaz, J., Villaseñor, A., Pulgar, J. A., & Quintana, L. (2015). From the North-Iberian Margin to the Alboran Basin: A lithosphere geo-transect across the Iberian Plate. *Tectonophysics, 663*, 399– 418. https://doi.org/10.1016/j.tecto.2015.07.009

Chalouan, A., & Michard, A. (1990), The Ghomaride nappes, Rif coastal range, Morocco: A Variscan chip in the alpine belt, *Tectonics, 9*, 1565–1583. https://doi.org/10.1029/TC009i006p01565

Chertova, M. V., Spakman, W., Geenen, T., van den Berg, A. P., & van Hinsbergen, D. J. J. (2014). Underpinning tectonic reconstructions of the western Mediterranean region with dynamic slab evolution from 3-D numerical modeling. *Journal of Geophysical Research: Solid Earth, 119*(7), 5876–5902. https://doi.org/10.1002/2014JB011150

Christensen, N. I., & Mooney, W. D. (1995). Seismic velocity structure and composition of the continental crust: A global view. *Journal of Geophysical Research: Solid Earth, 100*(B6), 9761– 9788. https://doi.org/10.1029/95jb00259

Clariana-García, M. P. Rubio-Pascual, F., Montes-Santiajo, M. J., & González-Clavijo, E. J. (2021). Mapa Geológico Digital continuo E. 1:50.000, Zona Centroibérica. Dominio esquisto-grauváquico y Cuenca del Guadiana (Zona-1400), GEODE. *Mapa Geológico Digital Conitnuo de España*, available at http://info.igme.es/cartografiadigital/geologica/geodezona.aspx?Id=Z1400 (last accessed March 2021).

Comas, M. C., García-Dueñas, V., & Jurado, M. J. (1992). Neogene tectonic evolution of the Alboran Sea from MCS data. *Geo-Marine Letters, 12*(2-3), 157-164. https://doi.org/10.1007/BF02084927

Crespo-Blanc, A., & Frizon de Lamotte, D. (2006). Structural evolution of the external zones derived from the Flysch trough and the South Iberian and Maghrebian paleomargins around the Gibraltar arc: a comparative study. *Bull. Soc. Géol. France, 177*(5), 267-282. https://doi.org/10.2113/gssgfbull.177.5.267

d'Acremont, E., Lafosse, M., Rabaute, A., Teurquety, G., Do Couto, D., Ercilla, G., Juan, C., Mercier de Lépinay, B., Lafuerza, S., Galindo-Zaldívar, J., Estrada, F., Vazquez, J. T., Leroy, S., Poort, J., Ammar, A., & Gorini, C. (2020). Polyphase tectonic evolution of fore-arc basin related to STEP fault as revealed by seismic reflection data from the Alboran Sea (W-mediterranean). *Tectonics, 39*(3). https://doi.org/10.1029/2019TC005885

De la Puente, J., Rodriguez, J. E., Monterrubio-Velasco, M., Rojas, O., & Folch, A. (2020). Urgent supercomputing of earthquakes: Use case for civil protection. In *Proceedings of the platform for advanced scientific computing conference (PASC '20)*. Association for Computing Machinery, New York, NY, USA. Article 9, 1-8. https://doi.org/10.1145/3394277.3401853

De Larouzière, F. D., Bolze, J., Bordet, P., Hernandez, J., Montenat, C., & d'Estevou, P. O. (1988). The Betic segment of the lithospereic trans-Alboran shear zone during the late Miocene. *Tectonophysic, 152*(1), 41-52. https://doi.org/10.1016/0040-1951(88)90028-5

DeMets, C., Iaffaldano, G., & Merkouriev, S. (2015). High-resolution Neogene and Quaternary estimates of Nubia-Eurasia-North America Plate motion. *Geophis., J. Int., 203*(1), 416–427. https://doi.org/10.1093/gji/ggv277

Díaz, J., & Gallart, J. (2009). Crustal structure beneath the Iberian Peninsula and surrounding waters: A new compilation of deep seismic sounding results. *Earth and Planetary Science Letters, 173*, 181– 190. https://doi.org/10.1016/j.pepi.2008.11.008

Diehl, T., Kissling, E., Herwegh, M., & Schmid, S. M. (2021). Improving absolute hypocenter accuracy with 3D Pg and Sg body-wave inversion procedures and application to earthquakes in the Central Alps region. *Journal of Geophysical Research: Solid Earth, 126*, e2021JB022155. https://doi.org/10.1029/2021JB022155

Echeverria, A., Khazaradze, G., Asensio, E., Gárate, J., Dávila, J. M., & Suriñach, E. (2013). Crustal deformation in eastern Betics from CuaTeNeo GPS network. *Tectonophysics, 608*, 600– 612. https://doi.org/10.1016/j.tecto.2013.08.020

Elliot, A. J., Oskin, M. E., Liu-Zeng, J., & Shao, Y. (2015). Rupture termination at restraining bends: The last great earthquake on the Altyn Tagh Fault. *Geophysical Research Letters, 42*(7), 2164-2170. https://doi.org/10.1002/2015GL063107

El Moudnib, L., Villaseñor, A., Harnafi, M., Gallart, J., Pazos, A., Serrano, I., Córdoba, D., Pulgar, J. A., Ibarra, P., & Himmi M. M. (2015). Crustal structure of the betic Rif system, Western Mediterranean, from local earthquake tomography. *Tectonophysics, 643*, 94-105, https://doi.org/10.1016/j.tecto.2014.12.015

Faccenna, C., Becker, T. W., Auer, L., Billi, A., Boschi, L., Brun, J. P., Capitanio, F. A., Funiciello, F., Horvàth, Jolivet, L., Piromallo, C., Royden, L., Rossetti, F., & Serpeloni, E. (2014). Mantle dynamics in the Mediterranean. *Reviews of Geophysics, 52*(3), 283-332. https://doi.org/10.1002/2013RG000444

Fernández-Ibáñez, F., & Soto, J. I. (2017). Pore pressure and stress regime in a thick extensional basin with active shale diapirism, Western Meditarranean. *AAPG (Am. Assoc. Pet. Geol.) Bull., 101*, 233-264. https://doi.org/10.1306/07131615228

Fernàndez, M., Torne, M., Vergés, J., Casciello, E., & Macchiavelli, C. (2019). Evidence of Segmentation in the Iberia-Africa Plate Boundary: A Jurassic Heritage? *Geosciences, 9*(8), https://doi.org/10.3390/geosciences9080343

Ferrater, M., Ortuño, M., Masana, E., Martínez-Díaz, J. J., Pallàs, R., Perea, H., Baize, S., García-Meléndez, E., Echeverria, A., Rockwell, T., Sharp, W., & Arrowsmith, R. (2017). Lateral slip rate of Alhama de Murcia fault (SE Iberian Peninsula) based on a morphotectonic analysis: comparison with paleoseismological data. *Quaternary International, 451*, 87-100. https://doi.org/10.1016/j.quaint.2017.02.018

Flanagan, M. P., Myers, S. C. & Koper, K. D. (2007), Regional travel-time uncertainty and seismic location improvement using a 3 dimensional a priori velocity model. *Bull. Seismol. Soc. Am., 97*, 804– 825. https://doi.org/10.1785/0120060079

Font, Y., Kao, H., Lallemand, S., Liu, C.-S., & Chiao, L.-Y. (2004). Hypocentre determination offshore of eastern Taiwan using the Maximum Intersection method. *Geophys. J. Int, 158*(2), 655– 675. https://doi.org/10.1111/j.1365-246X.2004.02317.x

Galindo-Zaldívar, J., González-Lodeiro, F., & Jabaloy, A. (1989). Progressive extensional shear structures in a detacthment contact in the western Sierra nevada (Betic Cordilleras, Spain). *Geodin. Acta, 3*(1), 73-85. https://doi.org/10.1080/09853111.1989.11105175

García-Castellanos, D., Fernàndez, M., & Torne, M. (2002). *Tectonics, 21*(3). 1-17. https://doi.org/10.1029/2001TC001339

García-Mayordomo, J. (2005). Caracterización y Análisis de Peligrosidad Sísmica en el Sureste de España. Ph.D. Thesis. Complutense University of Madrid. Madrid, Spain. 373 pp. (in Spanish).

GEBCO Compilation Group (2022) GEBCO_2022 Grid. (last accessed December 2022) https://doi.org/10.5285/e0f0bb80-ab44-2739-e053-6c86abc0289c

Giaconia, F., Booth-Rea, G., Ranero, C. R., Gràcia, E., Bartolome, R., Calahorrano, A., Lo Iacono, C., Vendrell, M. G., Cameselle, A. L., Costa, S., Gómez de la Peña, L., Martínez-Loriente, S., Perea, H., & Viñas, M. (2015). Compressional tectonic inversion of the Algero-Balearic basin: Latemost Miocene to present oblique convergence at the Palomares margin (Western Mediterranean). *Tectonics, 34*, 1516– 1543. https://doi.org/10.1002/2015TC003861

Gomez de la Peña, L., Grevemeyer, I., Kopp, H., Díaz, J., Gallart, J., Booth-Rea, G., Gràcia, E., & Ranero, C. R. (2020). The lithospheric structure of the Gibraltar Arc System from wide-angle seismic data. *Journal of Geophysical Research: Solid Earth, 125*(9), e2020JB019854. https://doi.org/10.1029/2020JB019854

Gómez de la Peña, L., Ranero, C. R., & Gràcia, E. (2018). The Crustal Domains of the Alboran Basin (Western Mediterranean). *Tectonics, 37*(10), 3352-3377. https://doi.org/10.1029/2017TC004946

Gómez de la Peña, L., Ranero, C. R., Gràcia, E., & Booth-Rea, G. (2021). The evolution of the westernmost Mediterranean basins. *Earth-Sci. Rev. 214*. https://doi.org/10.1016/j.earscirev.2020.103445

Gómez de la Peña, L., Ranero, C. R., Gràcia, E., Booth-Rea, G., Azañón, J. M., Tinivella, U., & Yelles-Chaouche, A. (2022). Evidence for a developing plate boundary in the western Mediterranean. *Nat. Commun., 13*, 4786. https://doi.org/10.1038/s41467-022-31895-z

Gómez-Novell,O., García-Mayordomo, J., Ortuño, M., Masana E., & Chartier, T. (2020) Fault System-Based Probabilistic Seismic Hazard Assessment of a Moderate Seismicity Region: The Eastern Betics Shear Zone (SE Spain). *Front. Earth Sci., 8*:579398. https://doi.org/10.3389/feart.2020.579398

Gràcia, E., Grevemeyer, I., Bartolomé, R., Perea, H., Martínez-Loriente, S., Gómez de la Peña, L., Villaseñor, A., Klinger, Y., Lo Iacono, C., Diez, S., Calahorrano, A., Camafort, M., Costa, S., d'Acremont, E., Rabaute, A., & Ranero, C. R. (2019). Earthquake crisis unveils the growth of an incipient continental fault system. *Nat. Commun., 10*(1), 1–11. https://doi.org/10.1038/s41467-019-11064-5

Grevemeyer, I., Gràcia, E., Villaseñor, A., Leuchters, W., & Watts, A. B. (2015). Seismicity and active tectonics in the Alboran Sea, western Mediterranean: Constraints from an offshore-onshore seismological network and swath bathymetry data. *Journal of Geophysical Research: Solid Earth, 121*, 767– 787. https://doi.org/10.1002/2015JB012073

Haberland, C., Gibert, L., Jurado, M. J., Stiller, M., Baumann-Wilke, M., Scott, G., & Mertz, D. F. (2017). Architecture and tectono-stratigraphic evolution of the intramontane Baza Basin (Betics, SE-Spain): Constraints from seismic imaging. *Tectonophysics, 709*, 69-84. https://doi.org/10.1016/j.tecto.2017.03.022

Herrero-Barbero, P., Álvarez-Gómez, J. A., Martínez-Díaz, J. J., & Klimowtiz, J. (2020). Neogene basin inversion and recent slip rate distribution of the northern termination of the Alhama de Murcia Fault (Eastern Betic Shear Zone, SE Spain). *Tectonics, 39*(7). https://doi.org/10.1029/2019TC005750

Herrero-Barbero, P., Álvarez-Gómez, J. A., Williams, C., Villamor, P., Insua-Arévalo, J. M., Alonso-Henar, J., & Martínez-Díaz, J. J. (2021). Physics-based earthquake simulations in slow-moving faults: A case study from the Eastern Betic Shear Zone (SE Iberian Peninsula). *Journal of Geophysical Research: Solid Earth, 126*(5), e2020JB021133. https://doi.org/10.1029/2020jb021133

Howarth, J., Barth, N., Fitzsimons, S., Richards-Dinger, K., Clark, K., Biasi, G., Cochran, U. A., Langridge, R. R., Berryman K. R., & Sutherland, R. (2021). Spatiotemporal clustering of great earthquakes on a transform fault controlled by geometry. *Nature Geoscience 14*, 314-320. https://doi.org/10.1038/s41561-021-00721-4

Husen, S., & Hardebeck, J. L. (2010). Earthquake location accuracy, Community Online Resource for Statistical Seismicity Analysis. https://doi.org/10.5078/corssa-55815573

Husen, S., Kissling, E., Deichmann, N., Wiemer, S., Giardini, D., & Baer, M. (2003). Probabilistic earthquake location in complex three-dimensional velocity models: Application to Switzerland. *Journal of Geophysical Research: Solid Earth, 108*(B2). https://doi.org/10.1029/2002JB001778

Instituto Geográfico Nacional (IGN). (2016). Informe de la actividad sísmica en el Mar de Alborán. Last Accessed December 2022. Available at: http://www.ign.es/web/resources/noticias/Terremoto_Alboran.pdf

Instituto Geográfico Nacional (IGN). (2020). The Spanish seismic catalog – Catálogo Sísmico Nacional. Spanish Seismic Network, International Federation of Digital Seismograph Networks, Dataset/Seismic network. Last Accessed December 2022. https://doi.org/10.7914/SN/ES

Instituto Geológico y Minero de España (IGME). (2017). SIGEOF – Geophysical Information System. Available in: http://info.igme.es/SIGEOF/

Instituto Geológico y Minero de España (IGME). (2021). Mapa Neotectónico 1:1.000.000 Instituto Geológico y Minero de España (IGME) y Empresa Nacional de Residuos Radiactivos (ENRESA). Authors: Castañón-Gómez, A., Baena-Pérez, J., Moreno-Serrano, F., Nozal-Martín, F., Alfaro-Zubero, J. A. & Barranco-Sanz, L. M. Last accessed December 2021 (in Spanish).

Instituto Geológico y Minero de España (IGME). (2022). QAFI: Quaternary Active Faults Database of Iberia. Last accessed December 2022, from IGME web site: https://info.igme.es/QAFI

Insua-Arévalo, J. M. (2008). Neotectónica y tectónica activa de la cuenca de Málaga (Cordillera Bética Occidental). Ph.D. Thesis. Complutense University of Madrid, Spain, 265 pp. (in Spanish).

Insua-Arévalo, J. M., García-Mayordomo, J., Salazar, A., Rodríguez-Escudero, E., Martín-Banda, R., Álvarez-Gómez, J. A., Canora, C., & Martínez-Díaz, J. J. (2015). Paleoseismological evidence of Holocene activity of the Los Tollos Fault (Murcia, SE Spain): A lately formed Quaternary tectonic feature of the Eastern Betic Shear Zone. *Journal of Iberian Geology, 41*(3). https://doi.org/10.5209/rev_JIGE.2015.v41.n3.49948

Jabaloy, A., Galindo-Zaldívar, J., & González-Lodeiro, F. (1993). The Alpujárride-Nevado-Filábride extensional shear zone, Betic Cordillera, SE Spain. *J. Struct. Geol., 15*(3), 555-569. https://doi.org/10.1016/0191-8141(93)90148-4

Jiménez-Pintor, J., Galindo-Zaldívar, J., Ruano, P., & Morales, J. (2002). Anomalías gravimétricas y magnéticas en la Depresión de Granada (Cordilleras Béticas): tratamiento e interpretación. *Geogaceta, 31*, 143-146 (in Spanish).

Kariche, J., Meghraoui, M., Timoulali, Y., Cetin, E., & Toussaint, R., (2018). The Al Hoceima earthquake sequence of 1994, 2004 and 2016: Stress transfer and poroelasticity in the Rif and Alboran Sea region. *Geophis., J. Int., 212*, 42-53. https://doi.org/10.1093/gji/ggx385

Lafosse, M., Gorini, C., Le Roy, P., Alonso, B., d'Acremont, E., Ercilla, E., Rabineau, M., Vázquez, J T., Rabaute, A., & Ammar, A. (2018). Late Pleistocene-Holocene history of a tectonically active segment of ht continental margin (Nekor basin, Western Mediterranean, Morocco). *Mar. Petrol. Geol., 97*, 370-389. https://doi.org/10.1016/j.marpetgeo.2018.07.022

Laske, G., Masters., G., Ma, Z. & Pasyanos, M. (2013) Update on CRUST1.0 - A 1-degree Global Model of Earth's Crust. *Geophys. Res. Abstracts, 15*, Abstract EGU2013-2658.

Leblanc, D. & Olivier, P. (1984) Role of Strike-Slip Faults in the Betic-Rifian Orogeny. *Tectonophysics, 101*, 345- 355. https://doi.org/10.1016/0040-1951(84)90120-3

Leonard, M. (2010). Earthquake fault scaling: Relating rupture length, width, average displacement, and moment release. *Bull. Seismol. Soc. Am., 100*(5A), 1971-1988. https://doi.org/10.1785/0120090189

Lomax, A., Virieux, J., Volant, P., & Berge-Thierry, C. (2000). Probabilistic earthquake location in 3-D and layered models, in *Advances in Seismic Event Location*. C. H. Thurber and N. Rabinowitz (Eds.), Dordrecht, Netherlands, 101-134. https://doi.org/10.1007/978-94-015-9536-0_5

Lomax, A., Michelini, A., & Curtis, A. (2014). Earthquake location, direct, global-search methods, in *Encyclopedia of Complexity and Systems Science*, Meyers R. A. (Ed.), Springer, New York, NY, 1-33. https://doi.org/10.1007/978-3-642-27737-5_150-2

Lomax, A., & Savvaidis, A. (2022). High-precision earthquake location using source-specific station terms and inter-event waveform similarity. *Journal of Geophysical Research: Solid Earth, 127*, e2021JB023190. https://doi.org/10.1029/2021JB023190

Lonergan, L., & White, N. (1997). Origin of the Betic-Rif mountain belt. *Tectonics, 16*(3), 504–522. https://doi.org/10.1029/96TC03937

López-Comino, J. A., Mancilla, F., Morales, J., & Stich, D. (2012). Rupture directivity of the 2011, Mw 5.2 Lorca earthquake (Spain). *Geophysical Research Letters, 39*(3). https://doi.org/10.1029/2011GL050498

Lozano, L., Cantavella, J. V., & Barco, J. (2020). A new 3-D P-wave velocity model for the Gulf of Cadiz and adjacent areas derived from controlled-source seismic data: application to nonlinear probabilistic relocation of moderate earthquakes. *Geophysical Journal International, 221*(1), 1–19. https://doi.org/10.1093/gji/ggz562

Mancilla, F. & Díaz, J. (2015). High resolution Moho topography map beneath Iberia and Northern Morocco from receiver function analysis. *Tectonophysics, 663*, 203-211. https://doi.org/10.1016/j.tecto.2015.06.017

Mancilla, F., Booth-Rea, G., Stich, D., Pérez-Peña, J. V., Morales, J., Azañón, J. M., Martín, R., & Giaconia, F. (2015a). Slab rupture and delamination under the Betics and Rif constrained from receiver functions. *Tectonophysics, 663*, 225-237. https://doi.org/10.1016/j.tecto.2015.06.028

Mancilla, F., Stich, D., Morales, J., Martín, R., Diaz, J., Pazos, A., Córdoba, D., Pulgar, J. A., Ibarra, P., Harnafi, M., & Gonzalez-Lodeiro, F. (2015b). Crustal thickness and images of the lithospheric discontinuities in the Gibraltar arc and surrounding areas. *Geophys. J. Int, 203*(3), 1804– 1820. https://doi.org/10.1093/gji/ggv390

Marín-Lechado, C., Pedrera, A., Peláez, J. A., Ruiz-Constán, A., González-Ramón, A., & Henares, J. (2017). Deformation style and controlling geodynamic processes at the eastern Guadalquivir foreland basin (Southern Spain). *Tectonics, 36*(5), 1072-1089. https://doi.org/10.1002/2017TC004556

Marín Lechado, C., Roldán García F.J., Pineda Velasco A., Martínez Zubieta P., Rodero Pérez, J., & Díaz Pinto, G.; Mapa Geológico Digital continuo E. 1: 50.000, Zonas internas de las Cordilleras Béticas. (Zona-2100). in GEODE. *Mapa Geológico Digital continuo de España*. Last accessed December 2021 (in Spanish). Available at: http://info.igme.es/cartografiadigital/geologica/geodezona.aspx?Id=Z2100

Martin-Banda, R., Insua-Arevalo, J. M. & Garcia-Mayordomo, J. (2021). Slip Rate Variation During the Last similar to 210 ka on a Slow Fault in a Transpressive Regime: The Carrascoy Fault (Eastern Betic Shear Zone, SE Spain). *Frontiers in Earth Science, 8*. https://www.frontiersin.org/articles/10.3389/feart.2020.599608

Martín-Serrano, A., Díaz de Neira J. A., Molinero Molinero, R., & Gómez Sainz de Aja, J. A. (2021) Mapa Geológico Digital continuo E. 1: 50.000, Zona Prebética y campo tabular del campo de Daimiel (Zona-1800). in GEODE. *Mapa Geológico Digital continuo de España*. Last accessed December 2021 (in Spanish). Available at: http://info.igme.es/cartografiadigital/geologica/geodezona.aspx?Id=Z1800

Martín, R., Stich, D., Morales, J., & Mancilla, F. (2015). Moment tensor solutions for the Iberian-Maghreb region during the IberArray deployment (2009-2013). *Tectonophysics, 663*, 261-274. https://doi.org/10.1016/j.tecto.2015.08.012

Martínez-Díaz, J. J., Alonso-Henar, J., Insua-Arévalo, J. M., Canora, C., García-Mayordomo, J., Rodríguez-Escudero, E., Álvarez-Gómez, J. A., Ferrater, M., Ortuño, M., & Masana, E. (2018). Geological evidences of surface rupture related to a seventeenth century destructive earthquake in Betic Cordillera (SE Spain): constraining the seismic hazard of the Alhama de Murcia fault. *Journal of Iberian Geology, 45*(1), 73–86.

Martínez-García, P., Comas, M., Lonergan, L., & Watts, A. B. (2017). From Extension to Shortening: Tectonic Inversion Distributed in Time and Space in the Alboran Sea, Western Mediterranean. *Tectonics, 36*(12), 2777-2805. https://doi.org/10.1002/2017TC004489

Martínez-Solares, J. M., & Mezcua-Rodríguez, J. (Eds.). (2002). Seismic Catalog of the Iberian Peninsula (880 B.C.–1900). Madrid, ES: IGN (in Spanish).

Matas, J. & Martín Parra, L.M. (2021a) Mapa Geológico Digital continuo E. 1: 50.000, Dominio de Obejo-Valsequillo de la Zona Centroibérica (Zona 2500). in GEODE. *Mapa Geológico Digital continuo de España*. Last accessed December 2021 (in Spanish). Available at: http://info.igme.es/cartografiadigital/geologica/geodezona.aspx?Id=Z2500

Matas, J. & Martín Parra, L.M. (2021b) Mapa Geológico Digital continuo E. 1: 50.000, Zona de Ossa-Morena (Zona 1500). in GEODE. *Mapa Geológico Digital continuo de España*. Last accessed December 2022 (in Spanish). Available at: http://info.igme.es/cartografiadigital/geologica/geodezona.aspx?Id=Z1500

Matos, C., Custódio, S., Batló, J., Zahradník, J., Arroucau, P., & Silveira, G. (2018). An Active Seismic Zone in Intraplate West Iberia Inferred From High-Resolution Geophysical Data. *Journal of Geophysical Research: Solid Earth, 123*(4). 2885-2907. https://doi.org/10.1002/2017JB015114

Mauffret, A., El-Robrini, M., & Gennesseaux, M. (1987). Indice de la compression recente en mer Mediterranee; un bassin losangique sur la marge nord-algerienne. *Bull. Soc. Géol. France, 3*(6), 1195-1206 (in French).

Medauri, M., Dévercère, J., Graindorge, D., Bracene, R., Badji, R., Ouabadi, A., Yelles-Chaouche, K., & Bendiab, F. (2014). The transition from Alboran to Algerian basins (Western Mediterranean Sea): Chronostratigraphy, deep crustal structure and tectonic evolution at the rear of a narrow slab rollback system. *Journal of Geodynamics, 77*, 186-205. https://doi.org/10.1016/j.jog.2014.01.003

Meijninger, B & Vissers, R. (2006). Miocene extensional basin development in the Betic Cordillera, SE Spain revealed through analysis of the Alhama de Murcia and Crevillente Faults. *Basin Research, 18*(4), 547-571. https://doi.org/10.1111/j.1365-2117.2006.00308.x

Mezcua, J., & Martínez-Solares, J. M. (1983). Sismicidad del área Ibero-Magrebí. Vol. 203, Instituto Geográfico Nacional, Madrid, Spain (in Spanish).

Montagner J. P. & Kennett B. L. N. (1995). How to reconcile body-wave and normal-mode reference Earth models? *Geophys. J. Int. 125*, 229-248. https://doi.org/10.17611/DP/9991801

Montenat, C. (1973). Les formations nèogenes et quaternaires du Levant Espagnol (Provinces d'Alicante et Murcia), Ph.D. Thesis, University of Orsay, France, 1170 pp. (in French).

Montenat, C. (1977). Les bassins néogènes du levant d'Alicante et de Murcia (Cordillères Bétiques Orientales Espagne. Stratigraphie, paleogeographie et évolution dynamique. Vol. 69, Laboratoire de Géologie de la Faculté des Sciences de l'Université de Lyon, Lyon, France, 345 pp. (in French).

Montenat, C. & d'Estevou, P. O. (1999). The diversity of late Neogene sedimentary basins generated by wrench faulting in the eastern Betic Cordillera, SE Spain. *Journal of Petroleum Geology, 22*(1), 61-80. https://doi.org/10.1111/j.1747-5457.1999.tb00459.x

Montes M., Salazar, A., Ramírez, J.I.; Nozal, F. & López Olmedo, F. (2021). Mapa Geológico Digital continuo E. 1:50.000, Zona Tajo-Mancha. (Zona 2400). in GEODE. *Mapa Geológico Digital continuo de España*. Last accessed December 2022 (in Spanish). Available at: http://info.igme.es/cartografiadigital/geologica/geodezona.aspx?Id=Z2400

Moreno, X., Gràcia, E., Bartolomé, R., Martínez-Loriente, S., Perea, H., Gómez de la Peña, L., Lo Iacono, C., Piñero, E., Pallàs, R., Masana, E., & Dañobeitia, J. J. (2016). Seismostratigraphy and tectonic architecture of the Carboneras Fault offshore based on multiscale seismic imaging: Implications for the Neogene evolution of the NE Alboran Sea. *Tectonophysics, 689*, 115–132. https://doi.org/10.1016/j.tecto.2016.02.018

NOAA National Geophysical Data Center. (2009). ETOPO1 1 Arc-Minute Global Relief Model. NOAA National Centers for Environmental Information (last accessed December 2022).

Oglesby, D. (2008). Rupture termination and jump on parallel offset faults. *Bull. Seismol. Soc. Am., 98*(1), 440-447. https://doi.org/10.1785/0120070163

Oglesby, D. & Mai, P. M. (2012). Fault geometry, rupture dynamics and ground motion from potential earthquakes on the North Anatolian Fault under the Sea of Marmara. *Geophysical Journal International, 188*(3), 1071-1087. https://doi.org/10.1111/j.1365-246X.2011.05289.x

Palomeras, I., Villaseñor, A., Thurner, S., Levander, A., Gallart, J., & Harnafi, M. (2017). Lithospheric structure of Iberia and Morocco using finite-frequency Rayleigh wave tomography from earthquakes and seismic ambient noise. *Geochem., Geophys., Geosys., 18*, 1824– 1840. https://doi.org/10.1002/2016GC006657

Pedrera, A., Ruiz-Constán, A., García-Senz, J., Azor, A., Marín-Lechado, C., Ayala, C:, Díaz de Neira, J. A., & Rodríguez-Fernández, L. R. (2020). Evolution of the South-Iberian

paleomargin: From hyperextension to continental subduction. *J. Struct. Geol., 148*. https://doi.org/10.1016/j.jsg.2020.104122

Piña-Valdés, J., Socquet, A., Beauval, C., Doin, M.-P., D'Agostino, N., & Shen, Z.-K. (2022). 3D GNSS Velocity Field Sheds Light on the Deformation Mechanisms in Europe: Effects of the Vertical Crustal Motion on the Distribution of Seismicity. *Journal of Geophysical Research: Solid Earth, 127*(6). https://doi.org/10.1029/2021JB023451

Podvin, P., & Lecomte, I. (1991). Finite difference computation of traveltimes in very contrasted velocity models: A massively parallel approach and its associated tools. *Geophys. J. Int, 105*(1), 271–284. https://doi.org/10.1111/j.1365-246X.1991.tb03461.x

Rodríguez-Escudero, E., Martínez-Díaz, J. J., Álvarez-Gómez, J. A., Insua-Arévalo, J. M., & Capote del Villar, R. (2014). Tectonic setting of the recent damaging seismic series in the Southeastern Betic Cordillera, Spain. *Bull. Earthq. Eng., 12*, 1831-1854. https://doi.org/10.1007/s10518-013-9551-3

Rodríguez-Escudero, E., Martínez-Díaz, J. J., Giber-Robles, J. L., Tsige, M., & Cuevas-Rodríguez, J. (2020). Pulverized quartz clasts in gouge of the Alhama de Murcia fault (Spain): evidence for coseismic clast pulverization in a matrix deformed by frictional sliding. *Geology, 48*(3), 283-287. https://doi.org/10.1130/G47007.1

Rodríguez-Fernández, J., Yesares.García, J., & Pérez-Peña, J. V. (2004). Informe sobre la Geología de Subsuelo de las Cuencas de Totana y Mar Menor. Instituto Geológico y Minero de España (IGME), Granada, Spain (in Spanish).

Roldán, F.J., Rodríguez-Fernández, J., Villalobos, M., Lastra, J., Díaz-Pinto, G., & Pérez Rodríguez, A.B. (2021) Mapa Geológico Digital continuo E. 1:50.000, Zonas: Subbético, Cuenca del Guadalquivir y Campo de Gibraltar. in GEODE. *Mapa Geológico Digital continuo de España*. Last accessed December 2022 (in Spanish). Available at: http://info.igme.es/cartografiadigital/geologica/geodezona.aspx?Id=Z2600

Royden, L. H. (1993). The tectonic expression slab pull at continental convergent boundaries. *Tectonics, 12*(2), 303-325. https://doi.org/10.1029/92TC02248

Sánchez-Roldán, J. L., Martínez-Díaz, J. J., Cantavella, J. V., Álvarez-Gómez, J. A., & Morales, & J. (2021). Relocation of Seismicity in the Guadalentín Tectonic Valley, Eastern Betics Shear Zone (Southeast Iberia). *Seismological Research Letters, 92*(5), 3046–3064. https://doi.org/10.1785/0220200341

Sanz de Galdeano, C., Delgado, J., Galindo-Zaldívar, J., Marín-Lechado, C., Alfaro, P., García-Tortosa, F. J., López-Garrido, A. C., & Gil, A. J. (2007). Anomalías gravimétricas de la cuenca de Guadix-Baza (Cordillera Bética, España). *Boletín Geológico y Minero, 118*(4), 763-774 (in Spanish).

Serpelloni, E., Vannucci, G., Pondrelli, S., Argnani, A., Casula, G., Anzidei, M., Baldi, P., & Gasperini, P. (2007). Kinematics of the western Africa-Eurasia plate boundary from local mechanisms and GPS data. *Geophys. J. Int., 169*(3), 1180-1200. https://doi.org/10.1111/j.1365-246X.2007.03367.x

Seton, M., Müller, R. D., Zahirovic, S., Gaina, C., Torsvik, T., Shepard, G., Talsma, A., Gurnis, M., Turner, M., Maus, S., & Chandler, M. (2012). Global continental and Ocean basin

reconstruction since 200 Ma. *Earth-Sci. Rev., 113*(3), 212-270. https://doi.org/10.1016/j.earscirev.2012.03.002

Silva, P. G., Goy, J. L., Somoza, L., Zazo, C., & Bardají, T. (1993). Landscape response to strike-slip faulting linked to collisional settings: Quaternary tectonics and basin formation in the Eastern Betics, southeastern Spain. *Tectonophysics, 224*(4). 289-303. https://doi.org/10.1016/0040-1951(93)90034-H

Silva, P. G., Mather, A. E., Goy, J. L., Zazo, C., & Harvey, A. M. (1996). Controles en el desarrollo y evolución del drenaje en zonas tectónicamente activas: el caso del río Mula (Región de Murcia, SE España). *Rev. Soc. Geo. España, 9*(3-4), 269-283.

Spakman, W., & Wortel, R. (2004). A tomographic view on western mediterranean geodynamics. In W. Cavazza, F. Roure, W. Spakman, G. M. Stampfli, & P. A. Ziegler (Eds.), *The TRANSMED Atlas. The Mediterranean region from crust to mantle: Geological and geophysical framework of the Mediterranean and the Surrounding areas* (pp. 31–52). Springer Berlin Heidelberg. https://doi.org/10.1007/978-3-642-18919-7_2

Stich, D., Ammon, C. H., & Morales, J. (2003). Moment tensor solutions for small and moderate earthquakes in the Ibero-Maghred region. *J. Geophys. Res., 108*(B3). https://doi.org/10.1029/2002JB002057

Stich, D., Serpelloni, E., Mancilla, F., & Morales, J. (2006), Kinematics of the Iberia-Maghreb plate contact from seismic moment tensors and GPS observations, *Tectonophysics, 426*(3–4), 295–317. https://doi.org/10.1016/j.tecto.2006.08.004

Stich, D., Martín, R., Morales, J., López-Comino, J. A. & Mancilla, F. (2020). Slip Partitioning in the 2016 Alboran Sea Earthquake Sequence (Western Mediterranean). *Front. Earth Sci., 8*:587356. https://doi.org/10.3389/feart.2020.587356

Theunissen, T., Chevrot, S., Sylvander, M., Monteiller, V., Calvet, M., Villaseñor, A., Benahmed, S., Pauchet, H., & Grimaud, F. (2018). Absolute earthquake locations using 3-D versus 1-D velocity models below a local seismic network: example from the Pyrenees. *Geophysical Journal International, 212*(3), 1806–1828. https://doi.org/10.1093/gji/ggx472

Thurber, C. H. (1992). Hypocenter-velocity structure coupling in local earthquake tomography. *Physics of the Earth and Planetary Interiors, 75*(1-3), 55-62. https://doi.org/10.1016/0031-9201(92)90117-E

Torne, M., Fernàndez, M., Vergés, J., Ayala, C., Salas, M. C., Jimenez-Munt, I., Buffet, G. G., & Díaz, J. (2015). Crust and mantle lithospheric structure of the Iberian Peninsula deduced from potential field modeling and thermal analysis. *Tectonophysics, 663*, 419– 433. https://doi.org/10.1016/j.tecto.2015.06.003

van Hinsbergen, D. J. J., Van Vissers, R. L. M., & Spakman, W. (2014). Origin and consequences of western Mediterranean subduction, rollback, and slab segmentation. *Tectonics, 33*(4), 393–419. https://doi.org/10.1002/2013TC003349

Viseras, C., Soria, J. M., Fernàndez, J., & García-García, F. (2005). The neogene-quaternary basins of the betic cordillera: an overview. *Geophysical Research Abstracts, 7*, 11123–11127.

Vissers, R. L. M., & Meijer, P. T. (2012). Iberian plate kinematics and Alpine collision in the Pyrenees. *Earth-Sci. Rev., 114*(1), 61-83. https://doi.org/10.1016/j.earscirev.2012.05.001

Völk, H. R. (1967). Relations between Neogene sedimentation and late orogenic movements in the Eastern Betic Cordilleras (SE Spain). *Geol. Mijnbouw., 46*(12), 471-474.

Weijermars, R. (1987). The Palomares brittle-ductile shear zone of southern Spain. *J. Struct. Geol., 9*(2), 149-157. https://doi.org/10.1016/0191-8141(87)90022-8

Wessel, P., Luis, J. F., Uieda, L., Scharroo, R., Wobbe, F., Smith, W. H. F., & Tian, D. (2019). The Generic Mapping Tools Version 6. *Geochem., Geophys., Geosys, 20*, 5556-5564. https://doi.org/10.1029/2019GC008515

Woodside, J. M., & Maldonado, A. (1992). Styles of compressional neotectonics in the Eastern Alboran Sea. *Geo-Marine Letters, 12*, 111-116. https://doi.org/10.1007/BF02084920

Zhou, H. (1994). Rapid three-dimensional hypocentral determination using a master station method. *Journal of Geophysical Research: Solid Earth, 99*(B8), 15439. https://doi.org/10.1029/94JB00934

Figure 1. Tectonic and geological setting of the westernmost Mediterranean (IGME, 2021). The rectangle within the regional map in the inset represents the area that covers mTAB3D. Two gray arrows represent the convergence direction between Iberia and Africa (Serpelloni et al., 2007). The main faults (red lines) are from QAFI v.4. Database (IGME, 2022). BSF: Bajo Segura fault; CrF: Crevillente fault; AMF: Alhama de Murcia fault; PF: Palomares fault; CbF: Carboneras fault; YF: Yusuf fault; AIF: Al-Idrisi fault; WAB: West Alboran Basin; EAB: East Alboran Basin; SAB: South Alboran Basin.

Figure 2. Map showing the distribution of data sources for building mTAB3D. The dashed rectangle frames mark the area covered in the model presented in Sánchez-Roldán et al. (2021). The depth cross sections depict the depth and lateral velocity variation of mTAB3D.

Figure 3. Absolute earthquake locations obtained with mIGN (a) and mTAB3D (b). Red triangles represent broad-band stations and accelerometers from the Spanish Seismic Network. The dashed square in Figure 3b shows the location of the Mula-Archena seismic sequence in 2018. The dashed red lines in the cross sections mark the 15 km depth. CrF: Crevillente fault, AMF: Alhama de Murcia fault; CF: Carrascoy fault; LTF: Los Tollos fault; PF: Palomares fault.

Figure 4. Maps showing the density of epicenters after relocations with mIGN1D (a) and mTAB3D (b). The scale bar represents the normalized number of epicenters per unit of area (10 km^2), and the map only shows those areas with density greater or equal to 5 epicenters / 10km^2.

Figure 5. Absolute earthquake locations obtained with mIGN (a) and mTAB3D (b) following the NLL-SSST procedure. The pink circles show the location of the three principal clusters, and the pink star depicts the Mw 6.3 mainquake of the sequence. The dashed red lines in the cross sections mark the 16 km depth. Red triangles represent broad-band stations and accelerometers from the Spanish Seismic Network. SAR: South Alboran Ridge; AIF: Al-Idrisi fault; TB: Tofiño-Xauen Bank; JF: Trougout fault; NF: Nekor fault.

Figure 6. Maps showing the density of epicenters after relocations with mIGN1D (a) and mTAB3D (b). The pink circles show the location of the three principal clusters. The scale bar represents the normalized number of epicenters per unit of area (10 km^2), and the map only shows those areas with density greater or equal to 5 epicenters / 10km^2 (contour lines every 10 events).

Figure 7. Detail map of the Mula-Archena seismic sequence during 2018 (Fig. 3b). (a): Epicentral distribution, as well as some faults and tectonic units. Black dashed lines delimit the hypocenters that are projected in the a-a' section. (b): Projected section (a-a') of the relocated hypocenters. The heatmap shows the density of events normalized to the number of events per 10 km^2 (contour lines every 10 events). The dashed line indicates the inferred boundary between the basement (pink) and sedimentary rocks (yellow). Focal mechanism of the Mw 3.9 mainshock from the moment tensor catalog of the Spanish Seismic Network (see Open Research section). LBF: Los Baños fault; MAF: Mula-Archena fault; TRF: Tollos-Rodeos fault; BqF: Barqueros fault; AMF: Alhama de Murcia fault.

Figure 8. Detail map of the Al-Hoceima seismic sequence during 2016 (Fig. 4). (a): Epicentral distribution and heatmap showing the areas with highest density of earthquakes. On the right

1084 panels, we include three depth sections projected across the principal clusters (6b, 6c, and 6d).
1085 The heatmaps show the density of events normalized to the number of events per 10 km^2
1086 (contour lines every 10 events). Focal mechanisms from Buforn et al. (2017) plotted at their
1087 original location. SAR: South Alboran Ridge; AIF: Al-Idrisi fault; TB: Tofiño-Xauen Bank; JF:
1088 Trougout fault.

1089 **Table 1.** Criteria for event location in NLL-SSST. Here, we show the residuals' root mean
1090 square, *t*he minimum number of readings, the maximum azimuthal gap, the P-arrival and S-
1091 arrival rms and the ellipsoid major semi-axis length.

1092 **Table 2.** Uncertainty values grouped in four subsets according to the number of arrivals used in
1093 the relocation for mIGN and mTAB3D (values in kilometers).

1094 **Table 3.** Uncertainty values grouped in four subsets according to the number of arrivals used in
1095 the relocation for mIGN and mTAB3D (values in kilometers).

Earth and Space Science

Supporting Information for

New 3D velocity model (mTAB3D) for absolute hypocenter location in southern Iberia and the westernmost Mediterranean.

José Luis Sánchez-Roldán[1], José A. Álvarez-Gómez[1], José J. Martínez-Díaz[1,2], Paula Herrero-Barbero[3], Hector Perea[4], Juan V. Cantavella[5], and Lucía Lozano[5]

[1]Department of Geodynamics, Stratigraphy and Paleontology, Complutense University of Madrid, Madrid, Spain.

[2]Geosciences Institute (IGEO-CSIC), Madrid, Spain.

[3]Geosciences Barcelona (GEO3BCN-CSIC), Barcelona, Spain.

[4]Institut de Ciències del Mar - CSIC, Barcelona, Spain.

[5]Spanish Seismic Network, Instituto Geográfico Nacional (IGN), Madrid, Spain.

Contents of this file

Additional Supporting Information (Files uploaded separately)

Introduction

Text S1 explains all the steps carried out to make the 3-D P-wave model (mTAB3D). Figures with information about the 3D-velocity model presented in this work (Fig. S1), the seismic stations used for the relocation (Fig. S2), VP/VS ratio (Figs. S3 & S5), and uncertainties (Figs. S4 & S6). Figure S4 shows additional information related to the Eastern Betics Shear Zone relocation, and Figure S7 compares different relocations for large earthquakes of the Al Hoceima seismic sequence. Table S1 summarizes the data used for building the 3-D P-wave local model (mTAB3D). Finally, Files S1 to S8 have the hypocentral solutions information of every relocation computed in this study.

Text S1.

The following lines explain how to model the structures and lateral heterogeneities in our study area to build the 3D P-wave velocity model. However, these steps can be replicated and used in other areas to obtain new 3D velocity models. We recommend using some GIS tools during the procedure.

Firstly, we gather every data related to the distribution and geometries of the tectonic units and structures within our study area. The most relevant works will be those that define, with enough resolution, the boundaries of sedimentary basins, basement surfaces, or the Moho. Also, the works that image boundaries between structures with contrasting properties, such as the case of sedimentary basins and basements bounded by faults. In Table S1 we show the data sources used in this work. To avoid possible boundary effects due to the outwards lack of data, we suggest setting a smaller model size, which will help to build the model using areas with similar data density. For example, although we gathered enough data to build a model within the approximate extension west: -7º, east: 2º, south: 34.5º and north: 40º, we finally cut our model extension to west: -6º, east: 1º, south: 35º and north: 39º.

After gathering the data, we group them depending on the category or subject of study to calculate the surfaces used in later steps. For example, we grouped those points that show values of the Moho depth into a specific category, those related to the basement top into another one, etc. Next, we obtain a 3D mesh (similar to a DTM) interpolating among points of the same category to create a surface (e.g.: Moho boundary, basement top, etc.). We chose the nearest neighbor interpolation method to make every 3D mesh. Then, we intersect these 3D meshes against horizontal layers separated every 1 km. We do this to extract the slice shapefiles every 1 km with the contour lines of that surface, which refers to the depth at which we found each surface of interest.

After completing all the slices, we cut them to their final maximum extension. Then, we calculate the intersection of the different surfaces at the same depth to define the geometry of the modeled units. For example, we make the geometry of a sedimentary basin by the intersection of the basement top surface and the topography surface (or bathymetry if it is an offshore sedimentary basin). This procedure is repeated slice by slice until we have completed every depth layer in our model. After this, we will obtain a set of shapefiles (as many as the desired depth of our model), where every shapefile is divided into different planar geometries. This division depends on the number of tectonic units at every depth layer. Readers should note that the model will be more complicated at the first depth layers since the data density is higher. The data availability will decrease progressively downwards, leading to less complex geometries.

We must estimate the P-wave velocity and its evolution in depth. This procedure implies a bibliographic review of the geologic composition and rheology of the type and features of rocks within the tectonic units of our study area. After this, if we know the average composition of the tectonic units, we can evaluate the P-wave velocity from empirical relations (Christensen & Mooney, 1995; Brocher, 2005) based on the density variation in depth. With these relations, we create individual velocity profiles (in km/s) for each tectonic unit in our model (Fig. S1).

After completing all the slices at every depth layer and all the velocity profiles, we select tectonic units within each slice shapefile and assign it its corresponding velocity value based on its particular profile estimated previously. As a result, we will obtain a slice shapefile divided into different units, where every tectonic unit will have a value that refers to the specific P-wave velocity at the depth of the slice.

When we complete the previous procedure for every depth slice, we sample each slice shapefile following a 1 km interval (both on the x-axis and y-axis). We will obtain points that will be extracted and saved in a text file with the following columns: "X", "Y", "Z" and "VP". The "X" and "Y" columns refer to the longitude and latitude coordinates (in degrees), respectively, the "Z" to the depth (in km) and the "VP" to the P-wave velocity at that point (in km/s). With that, we will create several files equal to the number of depth slices of our model, where each file contains the corresponding 3D coordinates and velocity value.

We will convert the coordinates from geographic to cartesian units. For this, we find the center point of the slice defined in the text file and set its geographic coordinates (longitude, latitude) to 0. For example, the center point of our model is longitude: -2.5º and latitude: 37º, so we need to change that to longitude: 0 and latitude: 0. Positive values will be located upwards and to the right, so the lower left corner of the slice would be X: -305 and Y: -221.

Finally, we can merge all the text converted text files and then compute .hdr and .buf files that we will need to calculate the travel times at each station using Grid2Time within Nonlinloc.

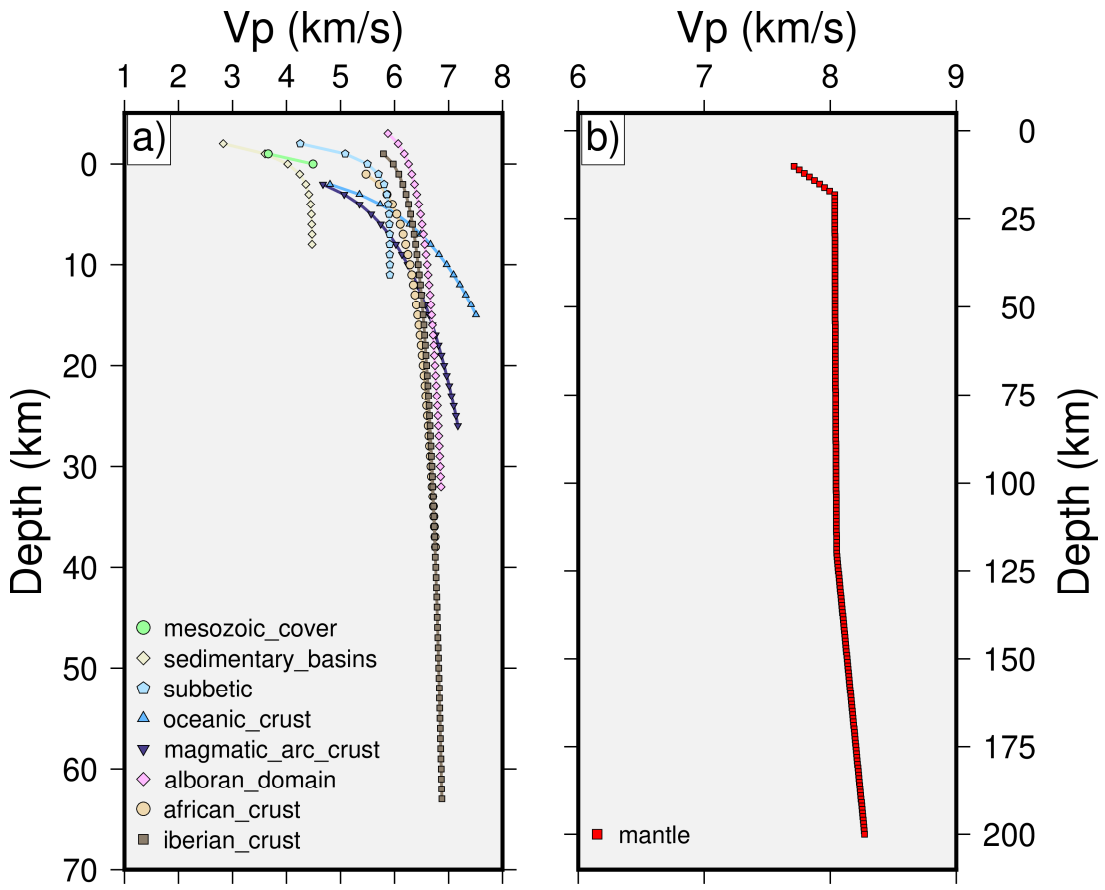

Figure S1. P-wave velocity profiles calculated for every crustal domain (a) and the mantle (b).

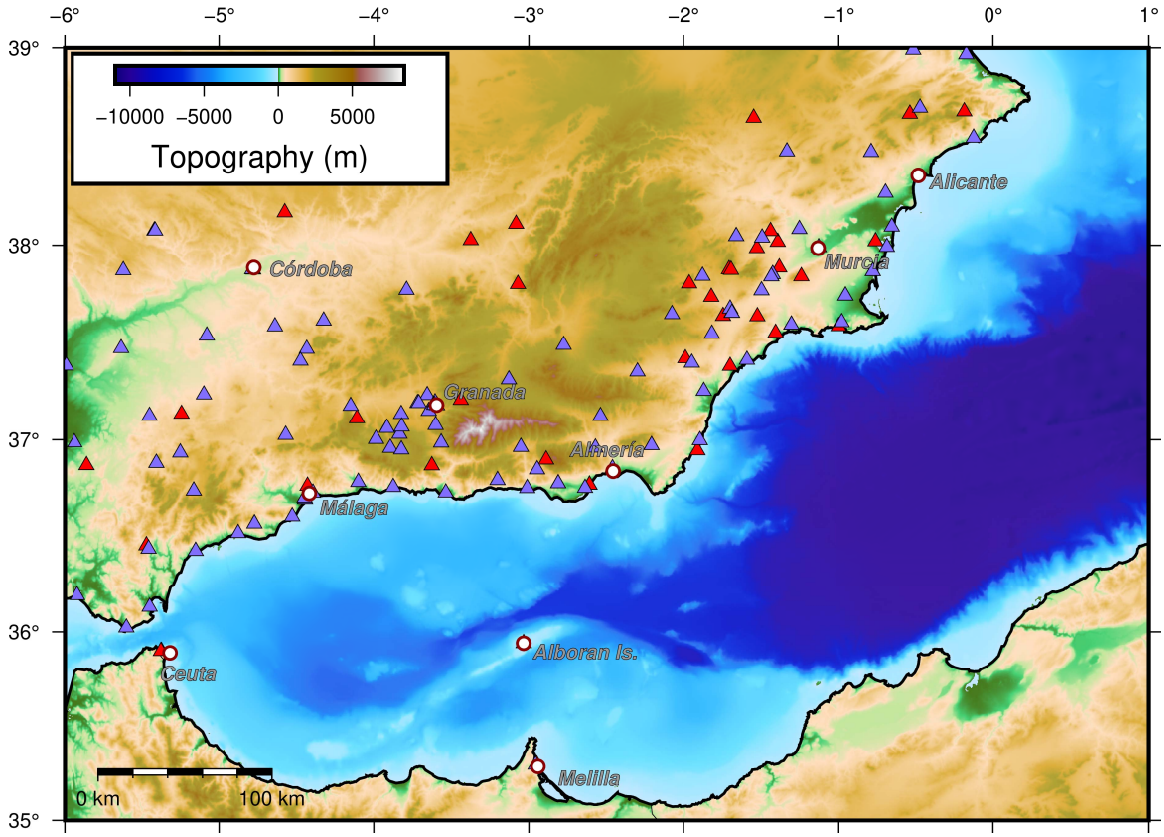

110

113 **Figure S2.** Elevation map of the study region showing the seismic stations used in this work
114 and their distribution (IGN, 2020). Red triangles: broad-band stations; purple triangles:
115 accelerometers.

114

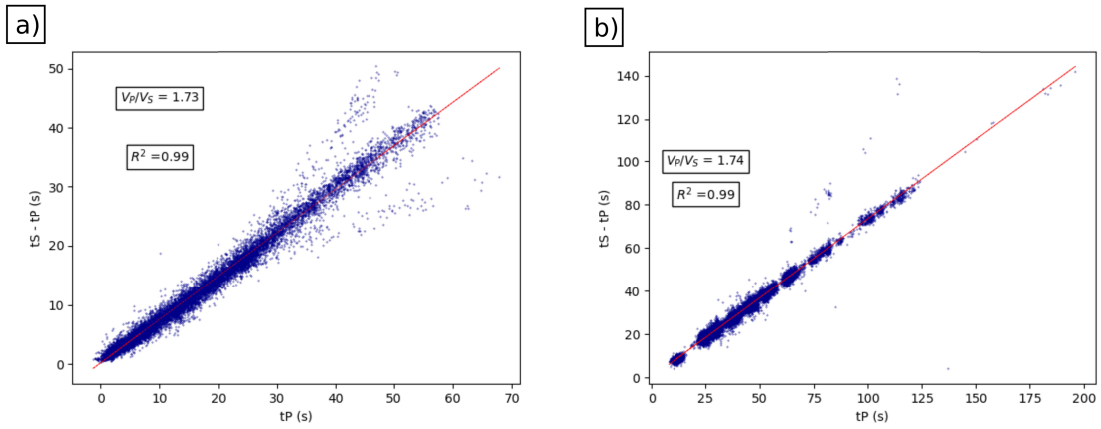

116 **Figure S3**. Wadati diagram comparing t_S-t_P values against t_P absolute for earthquakes in the
117 Eastern Betics Shear Zone (a) and the Alboran sea (b).

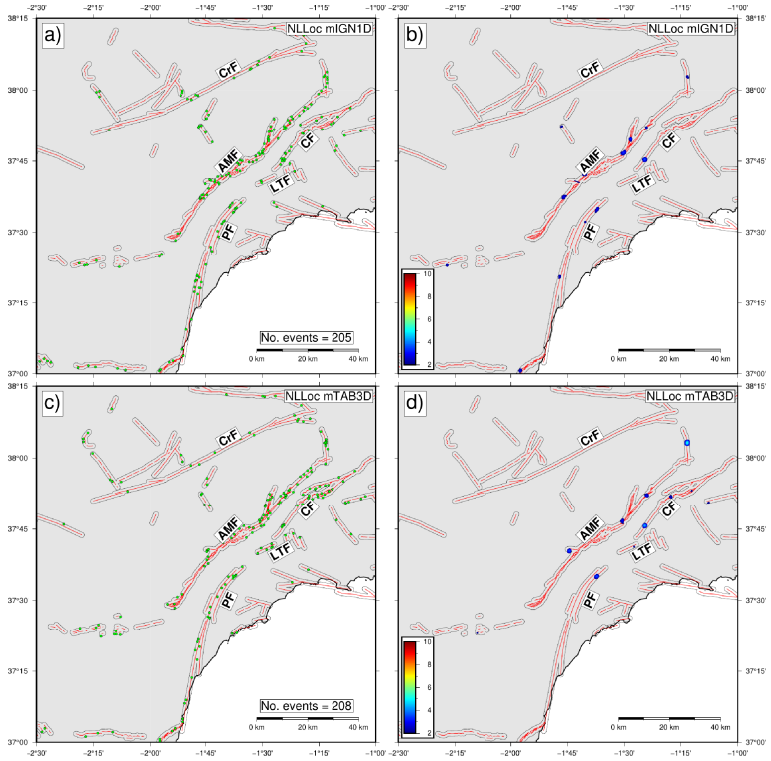

117

124 **Figure S4**. EBSZ 2018-2022 relocation results after using mIGN1D and mTAB3D. a, c: maps
125 showing the number and distribution of the hypocenters located closer than or at 1 km of the
126 traces of the main faults (black contours around the red lines). b, d: Density maps of the same
127 epicenters. The scale bar represents the normalized number of epicenters per unit of area (10
128 km^2), and the map only shows those areas with density greater or equal to 2 epicenters /
129 10km^2. CrF: Crevillente fault, AMF: Alhama de Murcia fault; CR: Carrascoy fault; LTF: Los Tollos
130 fault; PF: Palomares fault.

125

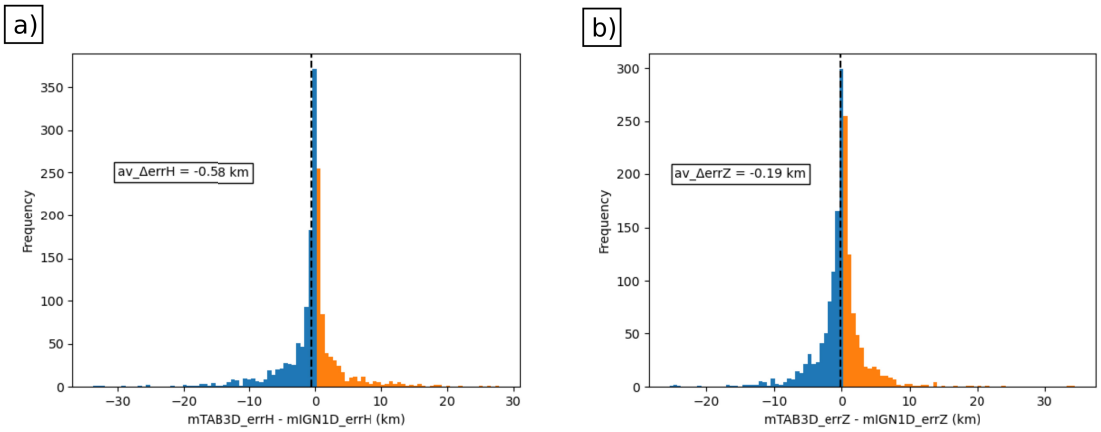

126

***Figure S5**. Histograms comparing errH (a) and errZ (b) earthquake by earthquake for Eastern Betics Shear Zone relocation. Values are obtained after subtracting mIGN1D uncertainty from mTAB3D uncertainty, thus negative values (blue color) imply that, for a specific earthquake, the result obtained using mIGN1D is worse than the one computed with mTAB3D, and vice-versa when referring to positive values (orange color). Black dashed line marks the error mean value.*

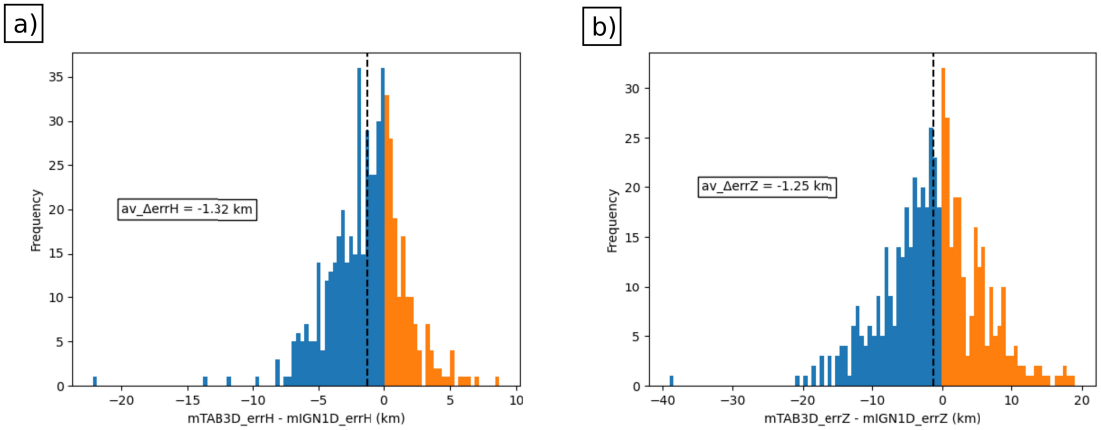

***Figure S6**. Histograms comparing errH (a) and errZ (b) earthquake by earthquake for Al Hocecima seismic sequence relocation. Values are obtained after subtracting mIGN1D uncertainty from mTAB3D uncertainty, thus negative values (blue color) imply that, for a specific earthquake, the result obtained using mIGN1D is worse than the one computed with mTAB3D, and vice-versa when referring to positive values (orange color). Black dashed line marks the error mean value.*

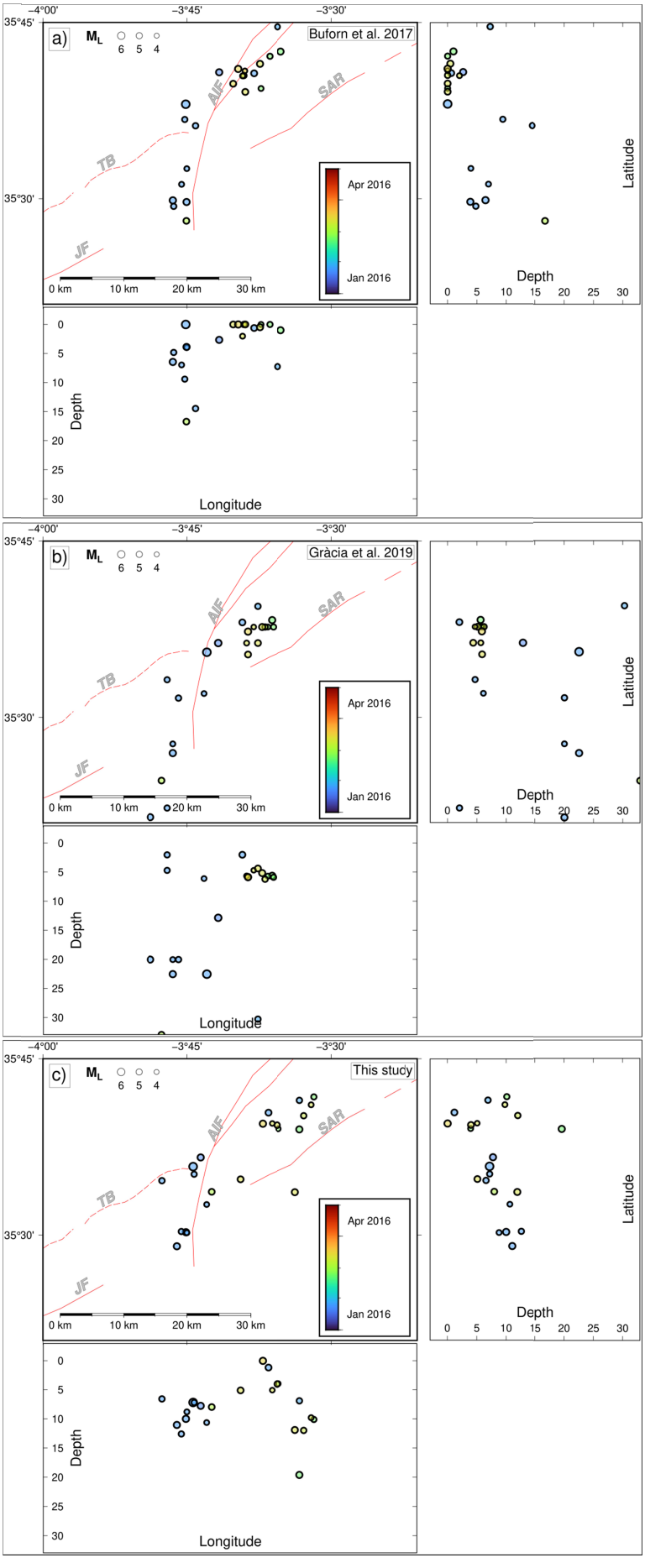
a)
Buforn et al. 2017
b)
Gràcia et al. 2019
c)
This study
ML
6 5 4
AJF
SAR
TB
JF
Apr 2016
Jan 2016
0 km 10 km 20 km 30 km
−4°00'
−3°45'
−3°30'
35°45'
35°30'
Depth
Latitude
Longitude
0 5 10 15 20 25 30

Figure S7. *Maps comparing the results after relocating the earthquakes of the Al-Hoceima seismic sequence with Mw>3.9 using different velocity models. (A) Hypocenters from Buforn et al. (2017) and 3D velocity model from El Moudnib et al. (2015). (B) Hypocenters from Gràcia et al. (2019) and local 1D velocity model from Grevemeyer et al. (2015). (C) Results presented in this study using mTAB3D. We can observe variations in hypocenter location and clustering. For example, results from Buforn et al. (2017) tend to locate very shallow earthquakes (<2 km in depth) in a cluster close to the AIF compressive step-over, whereas hypocenters from Gràcia et al. (2019) and our results are shifted to the east. Additionally, Gràcia et al. achieve a high clustering in this area between AIF and SAR. Results from Buforn et al. (2017) and this study show hypocenters around the southernmost end of AIF. However, hypocenters from Gràcia et al. (2019) are scattered around this zone and shifted southwards. While hypocenters from Buforn et al. (2017) and this study are restricted to the first ~20 km in depth, Gràcia et al. (2019) results show the wider depth range (from 2 km to 32 km) and high clustering around 5 km that seems to be related to a possible boundary within the 1D velocity model from Grevemeyer et al. (2015).*

155

Surface	Data	Source
Air/Water	Topography	NOAA National Geophysical Data Center (2009)
	Bathymetry	GEBCO Compilation Group (2022)
Neogene sedimentary basins	Seismic reflection profiles	Chevron and Enadimsa (http://info.igme.es/SIGEOF/) Medaouri et al. (2014) Marín-Lechado et al. (2017) Martínez-García, et al. (2017) Gómez de la Peña et al. (2018) d'Acremont et al. (2020) Gómez de la Peña et al. (2021)
	Gravity anomaly maps	Amores Lahidalga et al. (2002) García-Castellanos et al. (2002) Jiménez-Pintor et al. (2002) Rodríguez-Fernández et al. (2004) Sanz de Galdeano et al. (2007) Alfaro et al. (2008) Haberland et al. (2017) IGME (2017)
Basement (External/Internal zones and cover units)	Geological mapping from IGME	Clariana-García et al. (2021) Marín-Lechado et al. (2017) Martín-Serrano et al. (2021) Montes et al. (2021) Roldán et al. (2021)
	Receiver function studies	Mancilla et al. (2015) Mancilla and Díaz (2015)

Crustal thickness (Moho topography)	Deep seismic profiles	Carballo et al. (2015) Díaz and Gallart (2009) Booth-Rea et al. (2018) Gómez de la Peña et al. (2018) d'Acremont et al. (2020)
	Receiver functions	Mancilla et al. (2015)
	Ambient noise	Palomeras et al. (2017)
	Heat flow	Torne et al. (2015) Fernàndez et al. (1998)
	Gravity modeling	Insua-Arévalo (2008) Pedrera et al. (2020)

156 **Table S1.** Summary of the data used to build the 3-D P-wave velocity model mTAB3D. For each
157 layer we divide the table according the type of data and the source. Note that some sources
158 may appear more than once given that they were used for assessing two or more layers.
159

Files

We provide the eight files with the absolute locations and the uncertainty parameters (extracted from the 68% confidence ellipse of the PDF's) obtained after performing the relocation using mIGN1D and mTAB3D. The absolute location files follow this format:
origin_time(YYYY-mm-ddTDD:HH:MM) longitude(º) latitude(º) depth(km) magnitude(mbLg)

- origin_time: Hypocenter's origin time after the relocation.
- longitude: Hypocenter's longitude in decimal degrees after the relocation.
- latitude: Hypocenter's latitude in decimal degrees after the relocation.
- depth: Hypocenter's depth in kilometers.
- magnitude: Hypocenter's magnitude (mbLg) computed by the Spanish Seismic Network.

The files with the uncertainty values:
horizontal_uncertainty(km) vertical_uncertainty(km) rms(s) no_arrivals

- horizontal_uncertainty: Obtained after computing the geometrical mean between the horizontal semi-minor and semi-major axes of the 68% confidence ellipse in kilometers.
- vertical_uncertainty: Vertical semi-axis of the 68% confidence ellipse.
- rms: root-mean-square of residuals at maximum likelihood or expectation hypocenter.
- no_arrivals: number of readings used for the absolute location.

File S1. File_S1.dat: Eastern Betics Shear Zone catalog's absolute locations with mIGN1D.
File S2. File_S2.dat: Eastern Betics Shear Zone catalog's statistics with mIGN1D.
File S3. File_S3.dat: Eastern Betics Shear Zone catalog's absolute locations with mTAB3D.
File S4. File_S4.dat: Eastern Betics Shear Zone catalog's statistics with mTAB3D.
File S5. File_S5.dat: Al Hoceima 2016 catalog's absolute locations with mIGN1D.
File S6. File_S6.dat: Al Hoceima 2016 catalog's statistics with mIGN1D.
File S7. File_S7.dat: Al Hoceima 2016 catalog's absolute locations with mTAB3D.
File S8. File_S8.dat: Al Hoceima 2016 catalog's statistics with mTAB3D.